Thin Films: Heteroepitaxial Systems

edited by

Amy W.K. LIU

Quantum Epitaxial Designs, Inc.
119 Technology Drive, Bethlehem
Pennsylvania 18015, U.S.A.

and

Michael B. SANTOS

Department of Physics and Astronomy
University of Oklahoma
440 West Brooks, Norman
Oklahoma 73019, U.S.A.

World Scientific Publishing Co Pte Ltd
(Singapore, New Jersey, London)

Preface

Over the past two decades, the range of applications for epitaxial heterostructures has continually widened along with the steady introduction of new materials combinations. Artificially-structured materials can now be custom tailored for photonic applications across a large swath of the electromagnetic spectrum and electronic applications at frequencies approaching 100 gigahertz. To achieve a wide range of physical properties, the array of available component materials must be similarly diverse. Moreover, the usefulness of any single material is limited ultimately by our ability to create heterostructures that also contain other materials with complementary properties.

This volume presents a broad survey of the state-of-the-art in heteroepitaxy. Page restrictions have necessitated the regrettable omission of several important materials (such as silicides and narrow-gap II-VI semiconductors) and newly emerging topics (such as compliant substrates). Nevertheless, a nearly comprehensive coverage of heteroepitaxial topics is attempted. The first two chapters of this volume discuss issues that are fundamentally important in at least several materials systems that are discussed later. Chapters 3 through 6 cover non-semiconducting materials: metals, insulators, and superconductors. Chapters 9 through 13 cover group IV, III-V, II-VI, and IV-VI semiconductor systems. Each chapter is designed to be read without necessarily reading previous chapters. However, the reader is directed to other chapters in the volume when overlapping or related topics arise. This arrangement should appeal to graduate students and professionals who wish to come quickly up to speed on particular materials systems and to those who wish to study issues that connect many heteroepitaxial systems.

The selection of authors is purposely diverse. Some are well known for seminal achievements in their fields, while the others are younger scientists whose recent contributions reveal a broad knowledge of the forefronts of their fields. We hope that the reader profits equally from the vast experience of the former and the fresh outlook of the latter.

We would like to acknowledge the assistance of our colleagues at the University of Oklahoma, especially Kieran Mullen, Kory Goldammer and Andy Feldt. Special thanks to John Venables and Bruce Joyce, who not only contributed two excellent chapters, but also provided valuable advice on the content of this volume and carried out a critical reading of the manuscripts. Amy would like to thank her husband for his patient endurance and support of her preoccupation for the past 2 years, without which this endeavor would not have succeeded.

Amy W.K. Liu
Michael B. Santos
1998

Contents

Chapter 9

Molecular Beam Epitaxy of Sb-based Semiconductors

Brian R. BENNETT[a] and Benjamin V. SHANABROOK
Electronics Science and Technology Division, Naval Research Laboratory, Washington, DC 20375-5347, U.S.A.

9.1 Introduction

The growth of semiconductor antimonides by molecular beam epitaxy (MBE) was first reported in the late 1970's.[1,2,3] In recent years, the emergence of several potential device applications has resulted in increased activity in the field. Much of the work focuses on GaSb and AlSb because they are nearly lattice-matched to each other and to InAs ($a_{o,AlSb}$=6.1355 Å, $a_{o,GaSb}$=6.0954 Å, $a_{o,InAs}$=6.0584 Å). These semiconductors are often referred to as the "6.1 Å family." Ternaries such as $In_xGa_{1-x}Sb$, $AlAs_xSb_{1-x}$, and $GaAs_xSb_{1-x}$ also have lattice constants close to 6.1 Å if x is small. The interest in 6.1 Å materials is based upon the wide range of available band alignments and band gaps. These are illustrated in Fig. 9.1. For example, InAs is a small band-gap semiconductor ($E_{g,300K}$=0.36 eV) with a small electron effective mass (m_e=0.023m_o) and large room-temperature mobility (30,000 cm^2/V-s). Hence, it is a candidate for the channel material in high-speed field-effect transistors (FETs). AlSb is an indirect-gap semiconductor with a large band gap (1.63 eV). The conduction band offset between AlSb and InAs is 1.35 eV, making AlSb a potential barrier material for FETs. A second example is InAs/GaSb. The band alignment is type-II, with the GaSb valence band lying above the InAs conduction band. Short-period superlattices formed with InAs and GaSb have small, tunable energy gaps and high absorption coefficients. Hence, they are candidates for long-wavelength infrared detectors.

In Sec. 9.2 of this chapter we will discuss the growth of single layers of GaSb and AlSb. In particular, we will focus on issues of surface morphology, reconstructions, and self-assembled quantum dots. In Sec. 9.3 we will discuss Sb-based heterostructures. We will first address issues of critical layer thickness, growth temperature, and interfacial bonds. Then, we will look at four specific systems: InAs/AlSb superlattices, InAs/AlSb single quantum wells for FET applications, InAs/GaSb single quantum wells, and InAs/InGaSb super-

[a] Email: brian.bennett@nrl.navy.mil

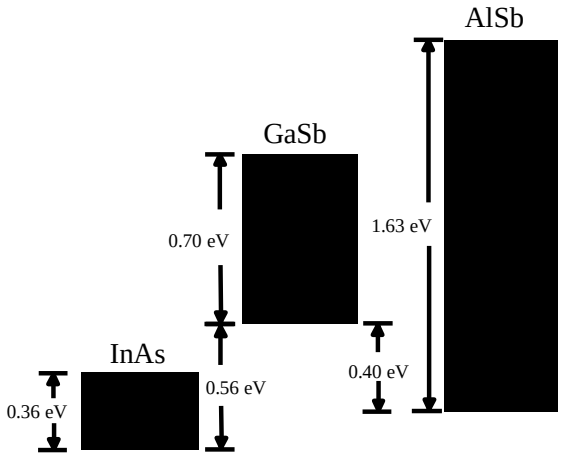

Figure 9.1: Band alignment of 6.1 Å III-V semiconductors (InAs, GaSb, and AlSb) at 300 K.

lattices for infrared detectors. In general, we will focus on the work of our group at the Naval Research Laboratory (NRL). Because of space limitations, several important topics will not be addressed here. These include MBE of InSb [4,5] and InSb-based heterostructures such as InSb/InAlSb,[6,7] (In,Ga,Al)As_xSb_{1-x} ternaries and quaternaries,[8] resonant tunneling diodes,[9] and infrared lasers.[10,11] Although MBE has been used in the majority of work in Sb-based thin-film epitaxy, important advances have also been reported using metal-organic chemical vapor deposition[12] but will not be discussed here.

9.2 Binary Layers

In this section, we will discuss the MBE growth of layers of binary semiconductors. First, we consider relatively thick layers of GaSb and AlSb. Then, we discuss the formation of self-assembled quantum dots at monolayer coverages of GaSb, AlSb, and InSb on GaAs substrates.

9.2.1 Surface Morphology, Reconstructions, and Transport

Currently, GaSb substrates are considerably more expensive than GaAs substrates. Highly resistive substrates of GaSb have not been achieved. In contrast, semi-insulating GaAs is readily available. For these reasons, much of the reported work on MBE of GaSb uses GaAs substrates. The lattice constant

of GaSb is 8% larger than that of GaAs. Hence, thick films of GaSb on GaAs always contain a high density of misfit dislocations.[13,14]

We used *in situ* scanning tunneling microscopy (STM) to examine the surface morphology of GaSb films on GaAs as a function of thickness.[15] Experiments were carried out in an interconnected, multi-chamber ultrahigh vacuum (UHV) facility that includes a III-V semiconductor MBE chamber and a surface analysis chamber with STM. The substrates were n^+GaAs, oriented to within 0.1° of (001). First, a GaAs buffer layer was grown at 580 °C. Next, the sample was cooled to 490 °C under an As_4 flux and GaSb was grown. The sample was then cooled to room temperature and transferred to the STM chamber. Images were acquired in constant-current mode with currents between 0.1 and 0.5 nA and sample biases ranging from -0.3 to -3.0 V.

In Fig. 9.2, we show the STM images after growth of 100 Å, 1000 Å, and 1.0 μm of GaSb on GaAs. At 100 Å (Fig. 9.2a), the surface is very rough, the result of 3D growth and the coalescence of islands. (The early stages of island growth will be discussed later.) After 1000 Å of GaSb (Fig. 9.2b), however, the surface is considerably smoother, with well-defined terrace edges. A large density ($\sim$50 μm^{-2}) of threading dislocations, including many dislocation half-loops, are seen emerging from the surface. As the film thickness increases, some of the dislocations annihilate one another. At a film thickness of 1.0 μm (Fig. 9.2c), the dislocation density is reduced to approximately 5 μm^{-2}. The film is growing in a spiral mode. Pyramidal structures are visible, with one or more threading dislocations emerging at the top and 500 Å-wide terraces winding down towards the bottom. Spirals of GaSb on GaAs were also observed by *ex situ* atomic force microscopy (AFM).[16,17] The terrace width increased with increasing growth temperature, presumably due to longer diffusion lengths for Ga atoms at higher temperatures.

In the case of GaSb homoepitaxy, a high density of threading dislocations is not expected. AFM observations of Brar *et al.*[17] as well as our own *in situ* STM measurements show no evidence of spiral growth. Instead, we observe mounds of GaSb on the surface, as shown in Fig. 9.3. These mounds consist of concentric growth rings, with each step equal to one monolayer (ML). The density of the mounds is a function of the quality of the starting substrate. For GaSb(001) from vendor A, we consistently observed mound densities of approximately $1\times10^8/cm^2$ (Fig. 9.3a). Substrates from vendor B, however, produced densities of only $4\times10^6/cm^2$ (Fig. 9.3b). Apparently, these mounds grow around imperfections in the starting substrate.

Subbanna *et al.* studied reflection high energy electron diffraction (RHEED) intensity oscillations for GaSb growth on GaAs substrates.[18] Oscillations are caused by periodic changes in the island density on the surface during

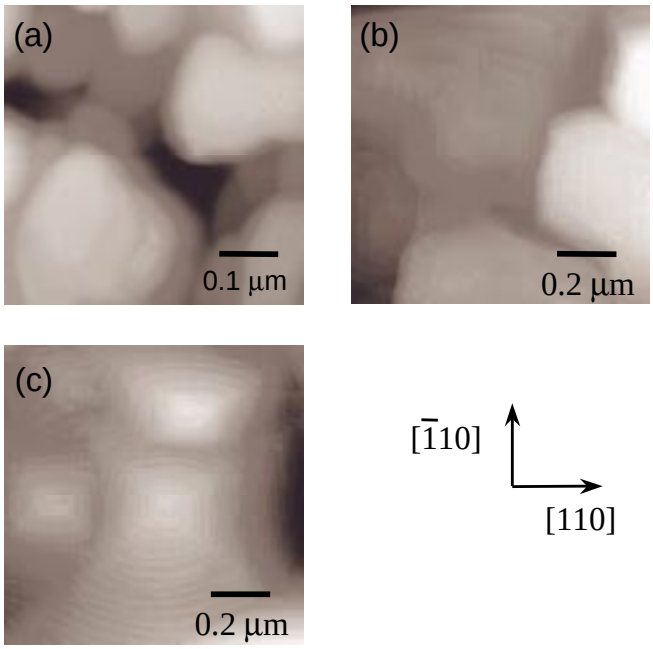

Figure 9.2: *In situ* STM images of GaSb on GaAs: (a) 100 Å thick (gray-scale range ≈500 Å), (b) 1000 Å thick (range≈100 Å), and (c) 1.0 μm thick (range≈60 Å).

growth, with each oscillation corresponding to the growth of one monolayer.[19] They observed oscillations for growth temperatures of 400–450 °C, but not at higher temperatures. We have confirmed these observations for GaSb on GaAs. During GaSb growth on high-quality (vendor B) GaSb substrates, however, we routinely observe RHEED oscillations at temperatures of 400–550 °C. These results can be explained in terms of step-flow growth. In the case of GaSb on GaAs, the entire surface is covered with spirals. The short terrace widths (200–500 Å) allow impinging Ga atoms to reach and incorporate into a terrace edge, resulting in step-flow growth with constant island density and an absence of RHEED oscillations for temperatures above 450 °C. The terrace widths are typically greater than 1000 Å on GaSb substrates, corresponding to a miscut of less than 0.2° from (001). As a result, most impinging Ga atoms cannot diffuse to a terrace edge, and instead form 2D islands on existing terraces, resulting in RHEED oscillations. We have also observed GaSb oscillations at temperatures of 500–550 °C when 30–50 Å GaSb caps are grown on a 4 μm AlSb/GaAs substrate. This result is consistent with large terraces

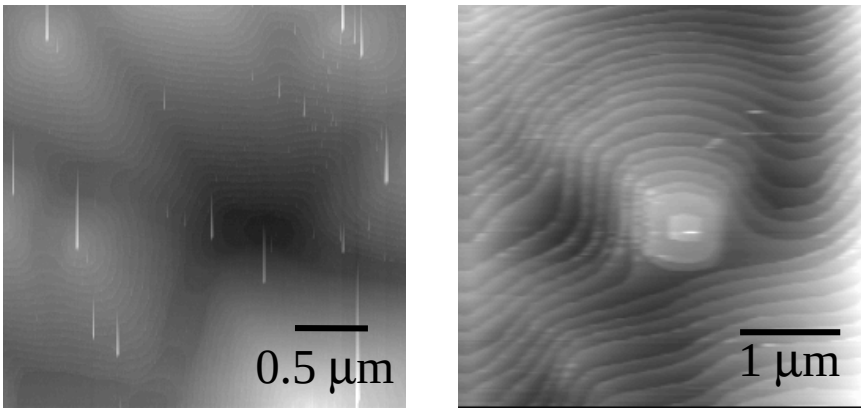

(a) (b)

Figure 9.3: *In situ* STM images of GaSb homoepitaxy: (a) MBE growth on GaSb (001) substrate from vendor A, (b) MBE growth on GaSb (001) substrate from vendor B. Monolayer terraces (∼3 Å) are visible on both samples.

on AlSb/GaAs structures.

Unintentionally doped GaSb layers grown by MBE are generally p-type with hole concentrations of 10^{16}–$10^{17}/\mathrm{cm}^3$.[20,21] Room-temperature and 77 K mobilities as large as 1000 and 6000 cm^2/V-s, respectively, have been reported. The native acceptor is generally thought to be an intrinsic defect, possibly Ga on an Sb site. Te is the most common n-type dopant. Because of the high vapor pressure of elemental Te, compounds such as GaTe and PbTe are usually used as sources. Controlled n-type doping in the 10^{15}–$10^{18}/\mathrm{cm}^3$ range has been achieved.[22,23]

Growth of AlSb on GaAs substrates has also been investigated by RHEED and STM. Subbanna *et al.* found that RHEED oscillations could be observed after as little as 350 Å of AlSb.[18] In contrast, much thicker layers of GaSb or InAs on GaAs are required before RHEED oscillations are observed. Our STM observations are consistent with the RHEED studies.[24] In Fig. 9.4, we show *in situ* STM images of 1000 Å films of AlSb on GaAs. The growth rate was constant at 1.0 ML/s and the temperature was varied as indicated, using Sb_4. In all cases, the surface is much smoother than 1000 Å of GaSb on GaAs (Fig. 9.2b). The optimum growth temperature is near 560 °C, with smaller terraces at lower temperatures and 100 Å-deep pits at 620 °C. A common practice for growth of 6.1 Å materials on GaAs is to first grow a 500–1000 Å nucleation layer of AlSb near 560 °C.

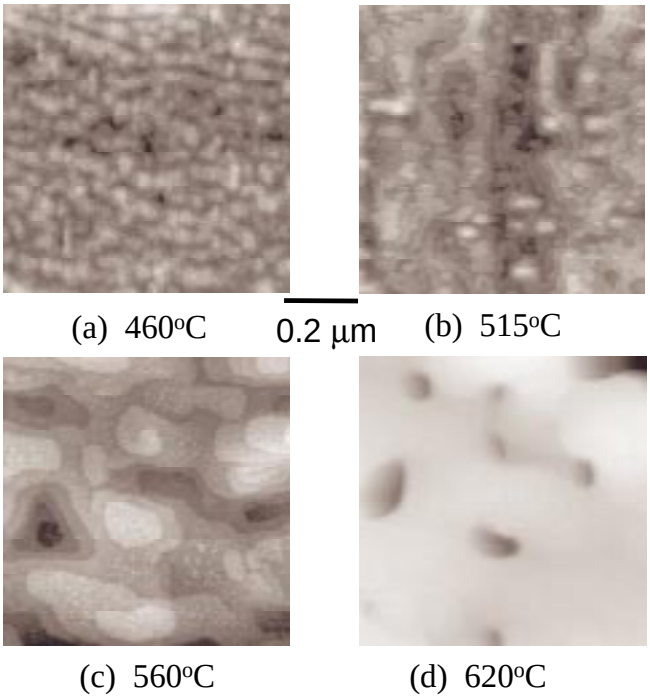

Figure 9.4: *In situ* STM images of 1000 Å films of AlSb on GaAs (001). The growth temperature of the AlSb is indicated for each sample. Monolayer (∼3 Å) terraces are visible on (a)–(c). The AlSb layer in (d) exhibits 100 Å-deep pits. (Reproduced with permission from Ref. [24].)

If growth is interrupted after several thousand angstroms of AlSb on GaAs, 100 or more RHEED oscillations can be routinely observed. In Fig. 9.5, we show RHEED data for AlSb grown at 500 °C on a GaAs substrate. The first set of oscillations was recorded following a 30 s growth interrupt under an Sb_4 flux. The interrupt time was reduced to 20, 10, and 5 s for subsequent growths. From the period of the oscillations, the growth rate is found to be 1.03 ML/s=3.16 Å/s=1.14 μm/hr. The intensity and duration of the oscillations are reduced when the interrupt time is reduced because the surface does not have sufficient time to form large terraces. A few oscillations were observed after interrupts of only 3 and 1 s (not shown). A beat phenomenon is superimposed on the oscillations. It results from lateral flux nonuniformities

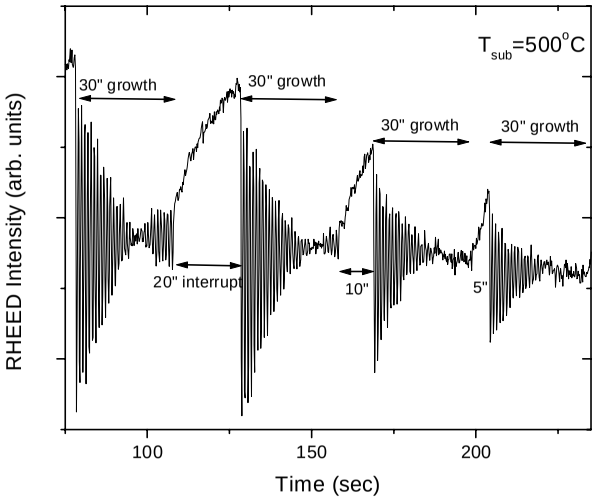

Figure 9.5: RHEED intensity recorded during the growth of AlSb. Strong oscillations are observed after growth interrupts.

across the sample.[25]

Recently, a new technique known as photoemission oscillations was introduced.[26] The periodicity of the oscillations corresponds to the growth rate. Apparently, photoemission oscillations, like RHEED oscillations, are related to fluctuations in the surface step density. They have been applied to measure growth rates of materials including AlSb and InAs. Photoemission oscillations can be measured during substrate rotation, allowing for immediate feedback to control layer thicknesses in structures such as resonant tunneling diodes.[27] The lattice constant of AlSb is 0.66% larger than that of GaSb. Hence, we expect a two-dimensional (2D) growth mode, with the formation of misfit dislocations to relieve strain. RHEED observations confirm this prediction, with no evidence of transmission spots during growth. STM measurements of a 1 μm film of AlSb on GaSb reveal a relatively smooth surface with clear monolayer terraces (Fig. 9.6).[28] In addition, we observe a classic cross-hatching pattern resulting from misfit dislocations oriented in the [110] and [$\bar{1}$10] directions.[29]

Little work has been reported on the transport properties of AlSb. Early work by Chang *et al.* achieved p-type AlSb (10^{15}–10^{19}/cm^3) under normal growth conditions using Ge as a dopant.[30] Under conditions of very high Sb flux, however, Ge was an n-type dopant. Si is also expected to be an amphoteric dopant in AlSb.[31] Under normal growth conditions, Si-doped layers are p-

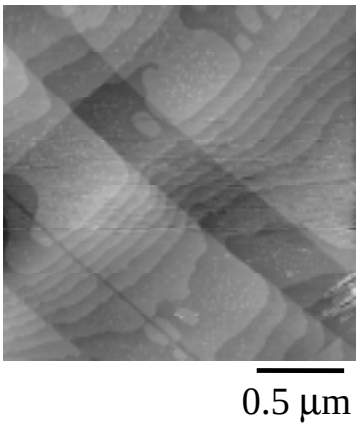

Figure 9.6: *In situ* STM image of 1 μm epitaxial layer of AlSb on GaSb(001). Monolayer ($\sim$3 Å) terraces and cross-hatch lines are present. (Reproduced with permission from Ref. [28].)

type. To develop a test of AlSb purity and avoid ambiguities associated with amphoteric dopants, we grew a series of thick layers of Be-doped AlSb on GaAs. The results are shown in Fig. 9.7. The room temperature mobility is indicated next to each data point. No corrections were made for depletion effects. The doping densities are comparable to GaAs(Be) layers grown with the same Be cell temperatures. As expected, mobilities generally increase with decreasing carrier density. Antimony sources were compared by growing two layers with T_{Be}=590 °C. For one, the antimony source was a conventional cell, yielding Sb_4. For the other, an antimony cracker was employed. The cracker zone temperature was 800 °C, probably resulting in a combination of Sb_2 and Sb_1.[32,33] As shown in Fig. 9.7, the layers have identical carrier concentrations and room-temperature mobilities. We also compared growth temperatures of 530 and 600 °C with T_{Be}=570 °C. The mobility and net carrier concentration were larger for the 600 °C sample, suggesting less incorporation of n-type impurities. The results in Fig. 9.7 imply a donor concentration of less than 10^{15}/cm^3 for AlSb in our MBE system.[34] Values reported in the literature are somewhat higher. Ideshita and Furukawa measured carrier concentrations in InAs/AlSb single quantum wells (SQWs) and obtained values of the donor concentration in AlSb of 1.5×10^{17}/cm^3 and 5×10^{15}/cm^3, depending upon the oxygen content of the source Sb.[35,36] Using similar test structures, Nguyen *et al.* found values of 2×10^{15} and 1.0×10^{16}/cm^3.[37]

Surface reconstructions of GaSb and AlSb have been studied by RHEED

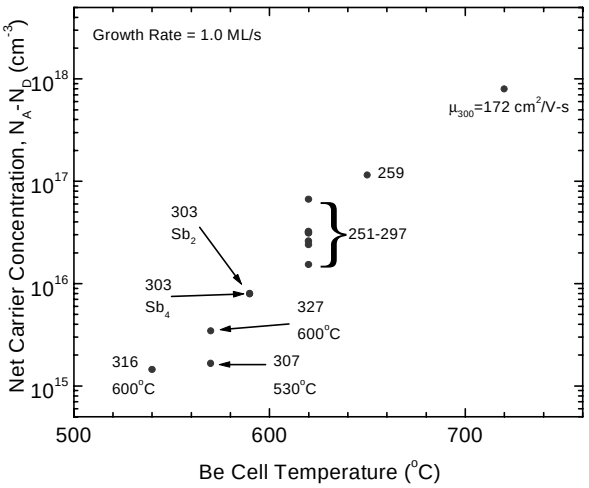

Figure 9.7: Net carrier concentration for thick layers of Be-doped AlSb on GaAs. Room-temperature hole mobilities are indicated for each sample. Unless otherwise noted, AlSb layers were grown at 530 °C using Sb_4. Epilayers were 3–5 μm thick except for the T_{Be}=540 °C sample which was 9 μm.

and x-ray photoelectron spectroscopy (XPS).[38,39,40,41,42,43,44] A GaSb surface under an Sb flux exhibits a (2×5) and/or c(2×10) reconstruction.[45] As temperature is increased, the reconstruction changes to c(2×6) and then (1×3). AlSb also reconstructs to a (1×3) surface at high temperatures. At lower temperatures, however, the reconstruction is c(4×4). In Fig. 9.8, we plot the reconstruction transitions under various Sb_4 and Sb_2 fluxes as a function of substrate temperature.[46] These transitions are often used as a method to estimate substrate temperature. Hysteresis effects are typically observed, with different transition temperatures for (2×5)→c(2×6) and c(2×6) →(2×5). In addition, we have found that the transition temperatures are affected by As contamination on the surface. Hence, this temperature measurement technique should be used with care.

9.2.2 Self-Assembled Quantum Dots

The Stranski-Krastanov (SK) growth mode in strained-layer heteroepitaxy has been recognized for decades.[47,48,49] In this mode, the deposited layer initially grows as a 2D wetting layer for at least one monolayer. Then, three-dimensional (3D) islands form on the wetting layer. Under appropriate growth conditions, these islands are isolated, coherent, and sufficiently small to be con-

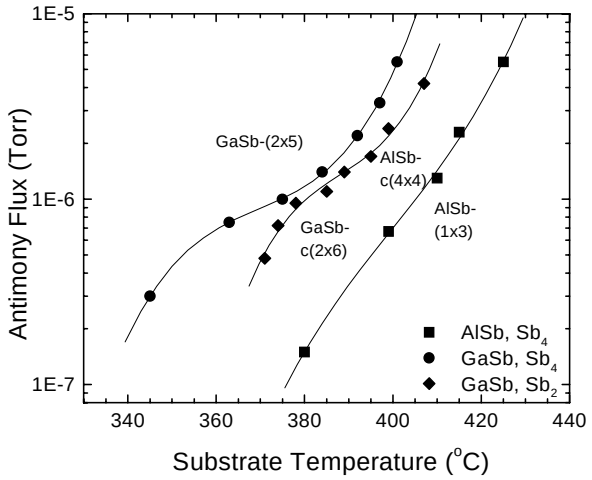

Figure 9.8: Surface reconstructions as a function of temperature and Sb_x flux for thick layers of GaSb and AlSb on GaAs substrates. Based upon GaSb RHEED oscillations, an Sb_4 flux of 1.4×10^{-6} Torr corresponds to 1.0 ML/s of Sb. Transition temperatures were determined by cooling the sample to below the transition and increasing temperature in 5 °C increments. Substrate temperatures were measured by GaAs transmission thermometry.

sidered quantum dots (QDs). Because no lithographic patterning is required, the QDs are said to be self-assembled. Recently, self-assembled QDs have been grown in a variety of semiconductor systems. A majority of the work has focussed on In(Ga)As/GaAs, InP/InGaP, and SiGe/Si. The reader is referred to review articles by Notzel [50] and Seifert *et al.*[51] and Ch. 8 in this book by Joyce and Vvedensky.[52] Here, we will discuss the growth and properties of InSb, GaSb, and AlSb QDs.

In 1990, Zhang *et al.* investigated the initial stages of MBE growth of InSb on GaAs.[53] Using RHEED and transmission electron microscopy (TEM), they observed faceted islands after deposition of 5 ML. The large distribution of island sizes suggests that the islands are not coherent at this coverage.[54] More recently, Watanabe *et al.* examined the growth of InSb on Se-terminated GaAs.[55] They observed InSb nanometer-size islands surrounded by (111) facets. In the last three years, at least four groups reported the growth and characterization of GaSb self-assembled QDs on GaAs.[56,57,58,59] In addition, we grew InSb and AlSb QDs directly on GaAs.[57] Other groups investigated the formation of InSb QDs on GaSb [60] and InP [61] substrates.

The growth procedures for QDs vary somewhat for different materials and research groups. In general, they begin with the growth of a smooth buffer layer

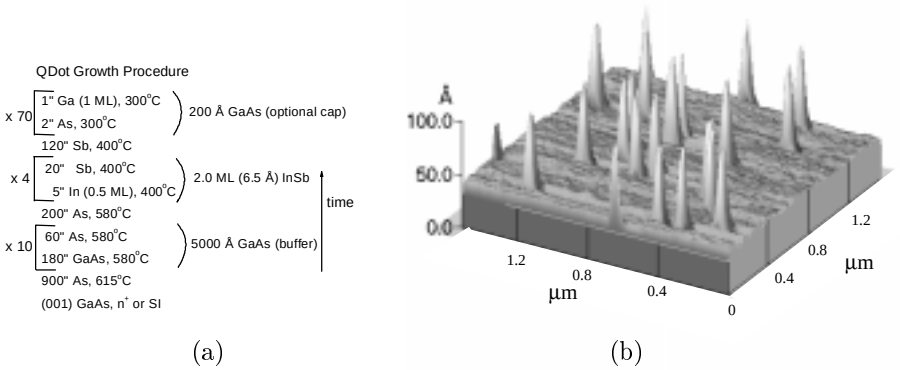

(a) (b)

Figure 9.9: (a) Growth procedure for 2.0 ML InSb on GaAs. (b) Ambient AFM image of 2 ML InSb on GaAs showing self-assembled quantum dots.

of GaAs, followed by the antimonide growth, usually at a relatively low rate. In our laboratory, samples were grown by solid-source MBE on semi-insulating or n^+ substrates, nominally oriented within 0.1° of (001). In Fig. 9.9a, we illustrate the QD growth procedure.

After oxide desorption, a GaAs buffer layer, 0.5–1.0 μm thick, is grown at 580 °C with interrupts and a growth rate of 1.0 ML/s. Growth is monitored by RHEED. During the GaAs buffer growth, the RHEED pattern is a streaky (2×4) reconstruction with no evidence of transmission spots. Before the growth of an antimonide layer, a 200 s growth interrupt under an As_4 flux at 580 °C is performed, resulting in sharp diffraction spots along each streak, indicating the formation of large terraces. Then, a well-ordered (2×4) or c(4×4) reconstruction is prepared using appropriate adjustments of substrate temperature and As_4 flux. After the interrupt, the substrate temperature is reduced and the valve for the arsenic source is closed to minimize As incorporation. The antimonide layer is grown by migration-enhanced epitaxy (MEE) with a cation deposition rate of 0.10 ML/s and a V:III flux ratio of approximately 2:1. (Growth rates are based upon RHEED oscillations during growth of thick epitaxial layers.) After deposition of the (In,Ga,Al)Sb monolayers, the sample is held at the growth temperature under an Sb_4 flux for 120 s before cooling. In the example shown in Fig. 9.9a, 2.0 MLs of InSb were grown. The standard growth temperature for InSb QDs was 400 °C. GaSb and AlSb QDs were typically grown near 500 °C. Selected samples were capped with GaAs to protect the QDs from oxidation. The cap layers, 100–300 Å thick, were grown by MEE at temperatures 100 °C below the growth temperature of the QDs. Cross-sectional TEM measurements reveal QDs after deposition of a cap.[62]

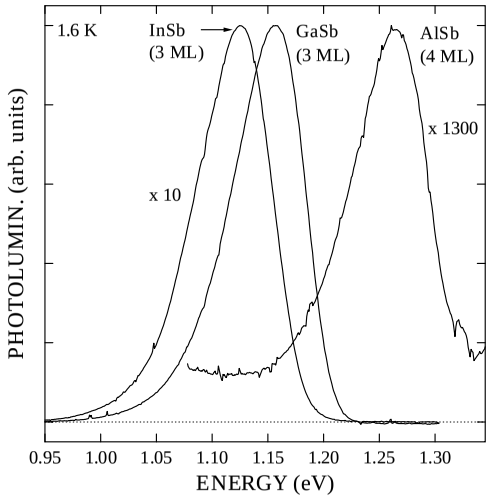

Figure 9.10: Photoluminescence spectra obtained at 1.6 K from 3 ML InSb, 3 ML GaSb, and 4 ML AlSb quantum dot samples (Power=2.8 W/cm^2).

Samples were characterized by AFM using silicon nitride cantilevers under ambient conditions; in addition, STM measurements were performed *in situ* as described earlier. AFM and STM scans of GaAs homoepitaxial layers prior to antimonide deposition reveal 3 Å monolayer steps and large smooth terraces with a lateral spacing of a few tenths of a micron. In Fig. 9.9b, we show a 1.5 μm by 1.5 μm AFM image of 2.0 ML InSb on GaAs-c(4×4). The density of QDs is approximately 10^9/cm^2, with typical heights of 82±5 Å and diameters of 760±70 Å. The fine details of a QD shape are unknown because the AFM image is a convolution of the true QD shape and the AFM tip geometry.

We characterized capped QD heterostructures by photoluminescence (PL) at 1.6 K, using the 4880 Å line from an Ar ion laser and a Ge detector cooled to 77 K. The PL spectra obtained under similar excitation power conditions (∼2.8 W/cm^2) from 3 ML InSb, 3 ML GaSb, and 4 ML AlSb QD samples are shown in Fig. 9.10.[63] Strong emission bands are observed from the InSb and GaSb QD samples with peak energies at 1.13 and 1.16 eV, respectively. The PL from the AlSb QDs is about three orders of magnitude weaker, with peak energy at 1.26 eV. (The composition of "AlSb" QDs will be discussed later.) The emission observed in the low- and high-energy wings of this band is due to recombination from the underlying GaAs substrate.

The emission peaks from the 3 ML InSb and GaSb QD samples occur at energies much larger than the low-temperature bulk InSb (0.24 eV) and GaSb

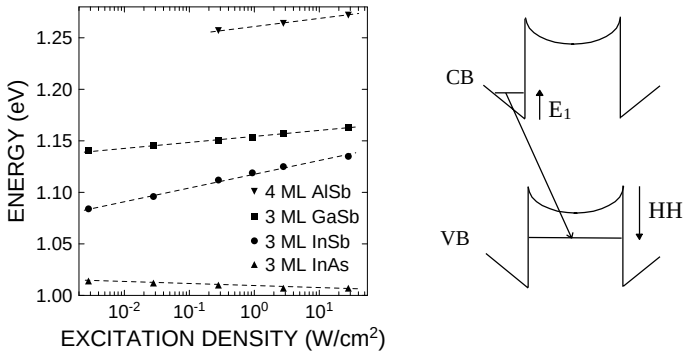

(a) (b)

Figure 9.11: (a) Peak energies of the PL emission bands from the InSb, GaSb, and AlSb quantum dot samples versus excitation power density. (b) Illustration of the band bending that occurs at interfaces of a heterostructure with type-II band alignment under high excitation power densities. (Reproduced with permission from Ref. [63].)

(0.81 eV) band gaps. However, the peak energy of the PL band observed from the 4 ML AlSb/GaAs QD heterostructure is smaller than the low-temperature AlSb indirect band gap (1.69 eV). This result suggests the possibility of a staggered or Type-II band alignment for AlSb QDs. Four experiments exploring the band alignments for all three materials are discussed next.

The luminescent properties of all three samples of Fig. 9.10 were investigated as a function of excitation power density. For comparison, a QD sample with 3 ML InAs on GaAs was also measured. The results are shown in Fig. 9.11a. The emission from the AlSb, GaSb, and InSb QDs shifts to higher energies with increasing excitation power density. In contrast, the emission band from the InAs QDs is almost independent of excitation power density. The behavior of the Sb QDs is consistent with a type-II band alignment, with electrons and holes separated in real space. Specifically, the peak shifts with power density for type-II structures due to the band bending that occurs at the interfaces (Fig. 9.11b). Thus, at high power densities, the resultant Hartree potential shifts the relative energies of the electron and hole states (E1 and HH1) and causes a shift of the PL band to higher energy. The weak excitation power dependence for InAs/GaAs QDs is consistent with a type-I band alignment.

Hatami *et al.* reported a similar result from excitation power studies of GaSb/GaAs QDs.[56] They obtained additional support for a type-II band alignment by investigating the temperature dependence of PL from GaSb QDs. The

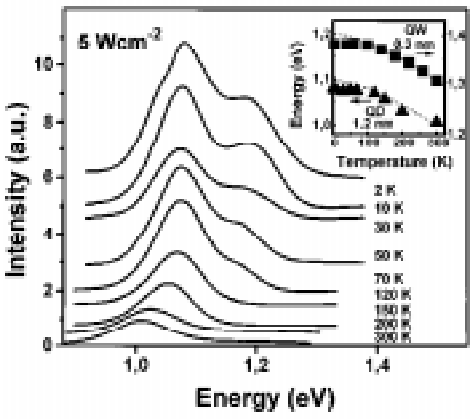

Figure 9.12: Temperature dependence of the PL spectra for a 12 Å GaSb quantum dot sample. The PL spectrum is dominated by the low-energy quantum dot line at temperatures above 100 K. At lower temperatures, a line attributed to the GaSb wetting layer is also observed. Inset: temperature dependence of the PL peak maximum in a 3 Å GaSb sample (quantum well, no dots) and the 12 Å QD sample. The dashed lines show the GaAs band gap versus temperature, shifted in energy scale. (Reproduced with permission from Ref. [56].)

results are shown in Fig. 9.12. At low temperatures, two bands are observed and attributed to the wetting layer (higher energy) and QDs.[64] The PL peaks follow the GaAs band-gap temperature dependence for T>130 K, but do not for lower temperatures (inset of Fig. 9.12), consistent with a type-II band alignment.

We investigated GaSb QDs in which the GaAs buffer and cap layers were replaced by $Al_{0.1}Ga_{0.9}As$ and $Al_{0.2}Ga_{0.8}As$. The resulting PL spectra are shown in Fig. 9.13. The peak energy increases as Al is added to the barrier layers. The expected shifts were estimated, assuming a type-II band lineup and applying the transitivity rule. A conduction-to-valence band offset ratio of 65:35 was used; small changes in hole confinement energies due to the expected heavy mass of holes in the GaSb QDs were assumed. The result is a predicted shift of 80 meV for each 10% change in AlAs mole fraction, in agreement with the experimental data.[63] We obtained similar results for InSb QDs clad by AlGaAs.

Sun *et al.* performed time-resolved PL measurements on GaSb QDs in GaAs.[58] They obtained time constants for the radiative decay process of 7–23 ns, compared to 600 ps for spatially direct GaSb/AlSb quantum wells. This result also supports the type-II band alignment model, with the longer time

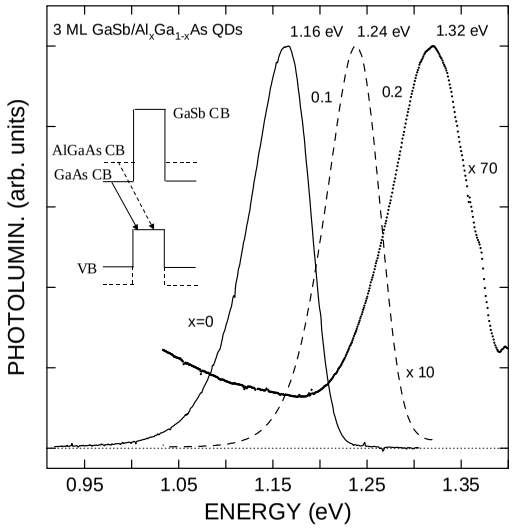

Figure 9.13: PL bands observed from 3 ML QD heterostructures grown with GaAs and AlGaAs barrier layers. Inset: schematic diagram of conduction- and valence-band minima and lowest-energy optical transitions for GaSb/GaAs and GaSb/AlGaAs QD structures. (Reproduced with permission from Ref. [63].)

constants for the QDs attributed to reduced spatial overlap between electron and hole wavefunctions. Rubin *et al.* applied ballistic electron microscopy to image individual GaSb quantum dots on GaAs and measured a local band offset of 80±20 meV.[65]

The chemical content of the QDs, as probed by the vibrational properties, was investigated with low-temperature Raman spectroscopy (RS).[66,67] RS data were collected at 4 K in the Z(X,Y)$\overline{Z}$ configuration where Z and $\overline{Z}$ are the directions of the incident and scattered light, (*,*) denote the directions of polarization of the incident and scattered radiation, and X, Y, and Z denote the [100] [010], and [001] crystallographic directions, respectively. Radiation from an Ar ion laser operating at 5145 Å was employed in the RS measurements.

In Fig. 9.14, we show the RS spectra for six samples. Samples with QDs were compared to control samples which included thin layers of antimonides but no QDs. As expected, the GaAs longitudinal-optic (LO) mode is present at 295 cm^{-1} for all samples. In addition, a second weak peak due to the GaAs transverse-optic (TO) mode is present at 271 cm^{-1}. The spectra for 3 ML GaSb grown directly on GaAs exhibits an additional peak at 234 cm^{-1}; AFM of this sample revealed QDs. This peak is absent for the 2 ML layer of GaSb

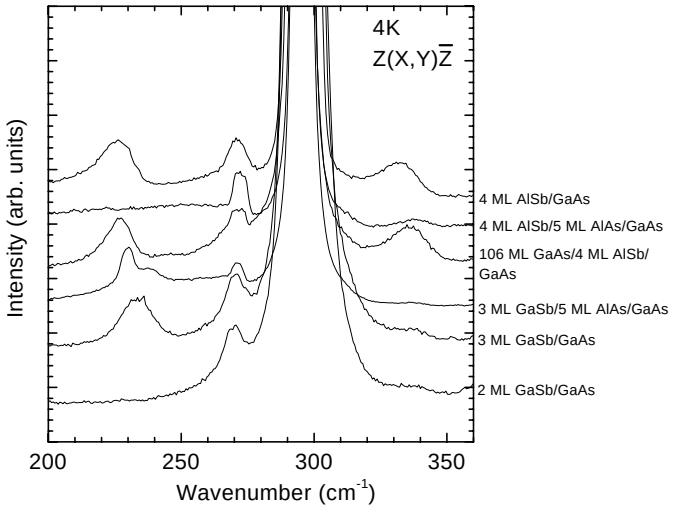

Figure 9.14: Low-temperature Raman spectra for six (Al,Ga)Sb samples. AFM revealed quantum dots for all samples except the 2 ML GaSb. Evidence for both GaSb-like (225–232 cm^{-1}) and AlSb-like (330–340 cm^{-1}) modes is observed. (Curves are offset for clarity.)

that does not have QDs. Because its energy lies between the energies of the LO (238 cm^{-1}) and TO (228 cm^{-1}) phonons in bulk GaSb, we attribute the 234 cm^{-1} peak to scattering from GaSb QDs. The absence of scattering from thinner layers of GaSb without QDs probably results from complete oxidation of the GaSb wetting layer. In the case of QDs, however, an unoxidized core of GaSb is expected in each QD.

QDs were not present after growth of 2 ML AlSb on GaAs. The RS spectrum (not shown) is nearly identical to 2 ML GaSb/GaAs or pure GaAs. After deposition of 4 ML AlSb, QDs are observed in AFM and additional scattering is present at 226 and 331 cm^{-1}. The high-energy peak lies between the LO (344 cm^{-1}) and TO (323 cm^{-1}) modes for bulk AlSb and the low-energy peak is only 8 cm^{-1} below the GaSb QD mode. Because of the similarity of this two-peak structure to the two-mode behavior observed in the vibrational properties of bulk AlGaSb alloys, we propose that the two peaks represent the two-mode behavior of phonons in $Al_xGa_{1-x}Sb$ QDs.[68] Presumably the alloying results from Ga segregation from the buffer layer into the QDs during growth. To confirm this hypothesis, we grew an additional sample consisting of 4 ML AlSb/5 ML AlAs/GaAs. AFM reveals QDs but the RS spectrum does not exhibit a GaSb-like mode, indicating the absence of GaSb in the QDs. The 5 ML

AlAs apparently acts as a barrier, preventing Ga segregation into the AlSb layer. The AlSb-like peak shifted to higher energy (338 cm^{-1}), but its intensity decreased. The direction of the peak shift is consistent with bulk AlGaSb alloys. As a rough estimate of QD composition, we used a linear interpolation, assuming the bulk values for changes in the AlSb-like (dE/dx=15 cm^{-1}) and GaSb-like (dE/dx=23 cm^{-1}) phonon energies, and assumed the 3 ML GaSb/GaAs and 4 ML AlSb/5 ML AlAs/GaAs samples consist of pure GaSb and AlSb QDs, respectively. For the sample with 4 ML AlSb/GaAs, we obtain a composition of $Al_{0.5}Ga_{0.5}Sb$ using the AlSb-like mode and $Al_{0.4}Ga_{0.6}Sb$ using the GaSb-like mode. We also examined a sample in which 5 ML AlAs was inserted between 3 ML GaSb and GaAs. As shown in Fig. 9.14, an AlSb-like mode is not present, suggesting that Al segregation into the GaSb is minimal, in agreement with the literature for AlAs/GaAs heterostructures. A double-peak is observed for the GaSb-like mode. This may represent LO and TO modes, as recently observed for InSb QDs on InP.[69]

To study the effect of capping layers, an additional sample was grown: 106 ML GaAs/4 ML AlSb/GaAs. The spectrum is similar to the uncapped sample, with two-mode behavior. The small changes in peak energies may be a result of different strain fields and alloy composition in the capped and uncapped QDs. Vibrational modes associated with InSb QDs were also reported.[66]

Although QDs with size uniformities on the order of 10% are routinely achieved, many potential applications such as solid-state lasers require more uniform ensembles of QDs. Theoretical work suggests that the uniformity of QDs is related to the structure of the wetting layer,[70,71] but few experimental studies have been reported. We applied *in situ* STM to investigate the structure of InSb, GaSb, and AlSb wetting layers on GaAs.[72] STM images of 1.5 ML InSb grown on GaAs-c(4×4) and GaAs-(2×4) reconstructions are shown in Figs. 9.15a and 9.15b, respectively. Larger area scans of both samples revealed quantum dots; the images in Fig. 9.15 are typical of areas between QDs. The wetting layers consist of highly anisotropic ribbon-like structures oriented along the [$\bar{1}$10] direction. The characteristic ribbon separation in the [110] direction, computed from autocorrelation functions, is 50 Å for growth on GaAs-c(4×4) and 40 Å for growth on GaAs-(2×4). The difference may be related to the As coverages: 1.75 ML for c(4×4) versus 0.5 ML for (2×4).

The traditional view of SK growth is that the initial deposition occurs as a continuous wetting layer. Our results, however, suggest a more complicated structure with a discontinuous morphology that may arise from a combination of effects. Both the relative surface energies of the absorbates and substrate, and the mismatch-related strain which may be relieved by the formation of vacancy lines, may play roles. A simple calculation, assuming complete strain

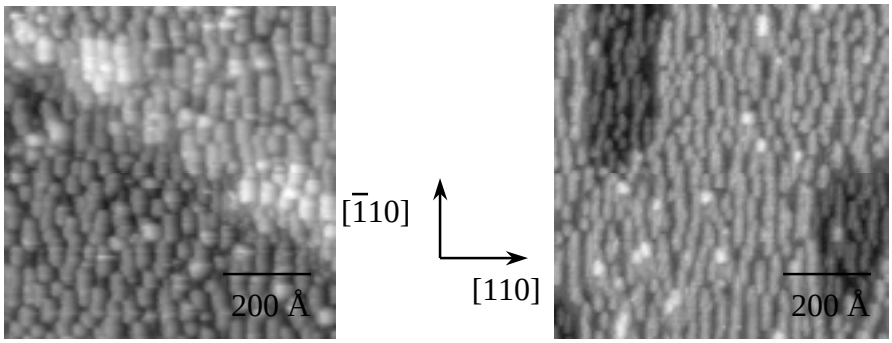

Figure 9.15: Filled-state *in situ* STM images of 1.5 ML of InSb on GaAs: (a) GaAs(001)-c(4×4) starting surface, (b) GaAs(001)-(2×4) starting surface. The gray-scale height ranges are approximately 12 Å. Images are taken from areas between quantum dots.

relaxation by vacancy arrays, gives a spacing of 6.8 atomic planes or 31 Å for InSb, compared to the experimental values of 40–50 Å.

The true shape of a QD is difficult to measure with STM or AFM due to tip convolution effects. RHEED patterns during QD formation often exhibit chevrons, indicative of faceting. Ferrer *et al.* examined InSb QDs on InP with high-resolution TEM and found a truncated pyramidal morphology, as shown in Fig. 9.16.[61] Images (a) and (b) are for samples of 5 ML and 7 ML InSb, respectively. The images reveal {111} lateral facets and an (001) top surface. A selected area diffraction pattern (not shown) exhibits splitting of the diffraction spots due to the 10% difference in lattice constant. The magnitude of the splitting indicates total strain relaxation.

9.3 Heterostructures

As discussed in Sec. 9.1, GaSb and AlSb are of interest because of the heterostructures that can be formed in the nearly lattice-matched InAs/GaSb/AlSb material system. In this section, we will first discuss three important issues that arise in the growth of these heterostructures: critical layer thickness, substrate temperature, and interfacial bonding. We will illustrate these factors by examining superlattices composed of alternating layers of InAs and AlSb. Then, we will discuss InAs/AlSb SQWs with applications as FETs, InAs/GaSb SQWs, and InAs/GaSb superlattices (SLs) for infrared detectors.

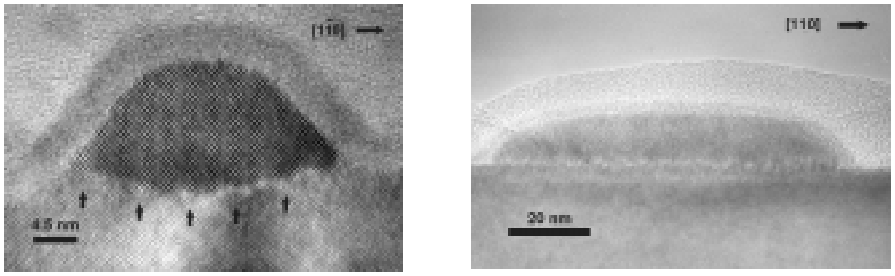

(a) (b)

Figure 9.16: High resolution [110] TEM images: (a) 5 ML InSb on InP (horizontal bar = 60 Å) and (b) 7 ML InSb on InP (horizontal bar = 200 Å), exhibiting preferential {111} lateral facets and (100) top surfaces and a network of misfit dislocations at the interface. (Reproduced with permission from Ref. [61].)

9.3.1 Strain and Critical Layer Thickness

Heteroepitaxy involves the growth of materials with different lattice constants, resulting in strain. There is a limit to the amount of strain that can be accommodated by epitaxial layers. If a layer is sufficiently thick and mismatched, the formation of misfit dislocations becomes energetically favorable. These dislocations relieve strain, but also degrade the structural, electrical, and optical quality of epitaxial layers, often making them unsuitable for device applications. For a fixed lattice mismatch, the thickness at which misfit dislocations begin to form is known as the critical layer thickness (CLT).

The classic "lattice-matched" semiconductor system is GaAs/AlAs with a lattice mismatch of only 0.14%. In practice, the formation of misfit dislocations in GaAs/AlGaAs heterostructures is almost never a problem. At the other extreme are systems with large mismatches such as Si/Ge (3.9%), GaAs/Si (4.0%), InSb/GaSb (6.1%), GaSb/GaAs (7.5%), and AlSb/GaAs (8.2%). Three-dimensional growth occurs for thin layers, with the formation of high densities of dislocations during the coalescence of islands, as discussed in Sec. 9.2.

Material combinations of interest here fall into an intermediate regime: AlSb/GaSb (0.66%), GaSb/InAs (0.61%), and AlSb/InAs (1.26%). Three-dimensional growth is not usually observed, but misfit dislocations will form if layers are sufficiently thick. The classic Matthews-Blakeslee[73] theory predicts critical thicknesses of approximately 200 Å for AlSb/GaSb or GaSb/InAs and 100 Å for AlSb/InAs. Although critical layer thickness is often considered in the design of device heterostructures for the 6.1 Å material system, few sys-

tematic studies have been reported. Gossmann *et al.* investigated single layers of AlSb grown on GaSb by MBE. Using x-ray diffraction and Raman scattering, they obtained CLTs of 50–170 Å.[74] Lazzari *et al.* examined LPE-grown layers of $Al_xGa_{1-x}As_ySb_{1-y}$ on GaSb.[75] They measured CLT by x-ray diffraction and found the values were different for layers in tension and compression, but always substantially larger than the Matthews-Blakeslee estimates. For example, compressively-strained layers with a mismatch of 0.2% had a CLT of 6000 Å.

We applied both single- and double-crystal x-ray diffraction (DCXRD) to a variety of InAs layers on GaSb substrates and buffer layers.[76] Layers were grown at a rate of 1.0 ML/s and a substrate temperature of 450 °C. Two types of samples were grown. The first was: InAs/GaSb/GaAs/GaAs(001)-substrate with the thickness of the strain-relaxed GaSb buffer layer ranging from 0.3–4.0 μm. The second was: InAs/GaSb/GaSb(001)-substrate, where high-quality(vendor B in Sec. 9.2.1) GaSb substrates were used.

A series of six samples was grown on GaSb substrates with InAs thickness varying from 500 Å to 1.0 μm. The (004) DCXRD measurements are shown in Fig. 9.17. For fully strained and fully relaxed InAs layers, the GaSb/InAs peak separation should be 1550 and 740 arc-sec, respectively. The classic behavior for mismatched epilayers is for the thinnest layers to be fully strained (coherent) up to a critical thickness, with increasing lattice relaxation (decreasing $\Delta\theta$) for increasing thickness beyond the critical value. To first order, that is what we observe in Fig. 9.17.[77] Substantial lattice relaxation does not occur until the layer thickness reaches 3000 Å, more than an order of magnitude larger than the Matthews-Blakeslee limit. As a result of limited resolution, DCXRD measurements are not sensitive to the onset of dislocation formation.[78] Hence, our results do not necessarily imply the absence of misfit dislocations for thinner layers.

Information about the epilayer quality can also be extracted from the data. The full-width at half-maximum (FWHM) is often cited as a measure of structural quality. Even for perfect layers, however, the FWHM is a function of thickness, with thinner layers having larger FWHMs because of the smaller correlation lengths. Hence, we use the ratio of the experimental to the theoretical FWHM as a figure-of-merit.[79,80] The FWHM ratios for the samples in Fig. 9.17 are: 1.1 (500 Å), 2.0 (1000 Å), 2.2 (2000 Å), 16 (3000 Å), 25 (5000 Å), and 41 (10000 Å). In addition, we observe Pendellosüing fringes for the 500 Å sample, indicating good structural quality.

The relaxation behavior of InAs layers grown on GaSb-buffer-layer/GaAs-substrate was considerably different. To summarize the data, we plot the epilayer strain as a function of InAs thickness in Fig. 9.18. The value of strain

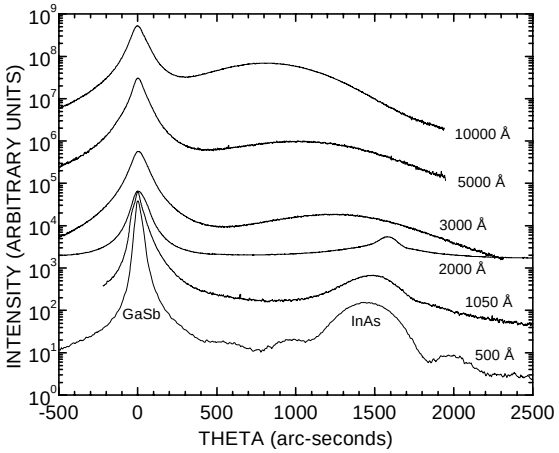

Figure 9.17: Double-crystal x-ray diffraction (004) rocking curves for epitaxial layers of InAs grown on GaSb(001) substrates. Substantial InAs lattice relaxation begins at a layer thickness of 3000 Å. (Curves are offset for clarity.)

should be 0.61% for a coherent layer. In general, layers on GaAs substrates are more relaxed than those on GaSb substrates. For example, at a thickness of 2000 Å, InAs on a GaSb substrate is fully strained, but the strain drops to 0.2–0.4% for GaSb buffer layers on GaAs substrates. In addition, more strain is retained in the InAs layer when the GaSb buffer layer is thicker.

These results are consistent with threading dislocations serving as nucleation sites for misfit dislocations. In the case of GaSb buffer layers on GaAs, high densities of threading dislocations form during the coalescence of islands. The dislocation density decreases as layer thickness increases. Hence, fewer nucleation sites will be available for thicker buffer layers, resulting in less relaxation of the InAs. The lowest density of threading dislocations is expected for the GaSb substrates, with etch pit densities less than $10^4/\mathrm{cm}^2$. We note that in the InGaAs/GaAs system, the density of misfit dislocations in the strained InGaAs was found to be a function of the density of threading dislocations in the GaAs substrate.[81,82] In summary, the strain in an epilayer can be a strong function of the quality of the underlying layer. To minimize lattice relaxation in InAs, very thick buffer layers of GaSb or, if possible, GaSb substrates should be used.

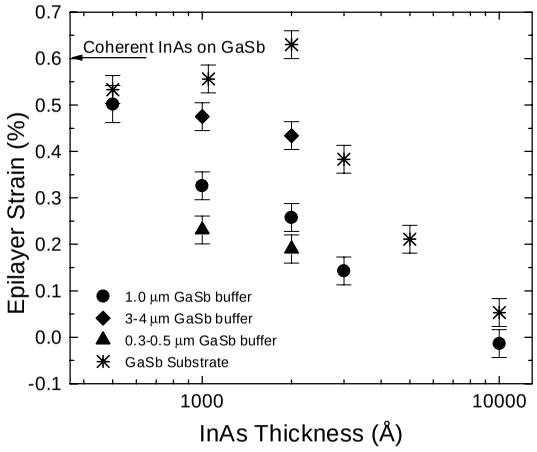

Figure 9.18: InAs epilayer strain as a function of layer thickness for the samples of Fig. 9.17 (InAs on GaSb substrates) as well as samples of InAs grown on GaAs substrates with GaSb buffer layers.

9.3.2 Growth Temperature

Before discussing the appropriate growth temperatures for 6.1 Å heterostructures, we will address a complication that can occur when In-free substrate holders are used in MBE. If a small band gap material (e.g. GaSb) is grown on a larger band gap material (e.g. GaAs) the increased absorption of radiation from the substrate heater can result in as much as a 150 °C increase in temperature without a change in the thermocouple reading.[83,84] We have observed this increase by measuring the substrate temperature via transmission thermometry. In this technique, radiation from the substrate heater passes through the GaAs substrate and is collected through a bakeable window and optical fiber. It is then passed through a spectrometer, allowing determination of the absorption edge and hence the band gap and temperature of the GaAs.[83] We applied this technique to all of our samples discussed in this chapter that were grown on GaAs substrates. The (1×5) to (1×3) reconstruction transition discussed in Sec. 9.2.1 was used for estimating temperature on GaSb substrates.

The congruent sublimation temperatures are 480 °C for GaSb [85] and 600 °C for AlSb. Reported values for InAs range from 370 to 500 °C.[85,86] High-quality AlSb can be grown at 600 °C (see Fig. 9.7), but InAs cannot be grown at such elevated temperatures. Hence, the optimal growth temperature for heterostructures of InAs, GaSb, and AlSb is not obvious. In general, more intermixing at interfaces is expected at higher growth temperatures. Yano

et al. addressed the issue of interfacial abruptness by subjecting 1μm layers of (In,Ga,Al)As to Sb_4 beams and (In,Ga,Al)Sb to As_4 beams as a function of temperature.[85] They determined surface stability by examining RHEED reconstructions and looking for new compounds with Raman spectroscopy. For example, a GaSb surface subjected to an As_4 beam for 1800 s exhibited GaAs-like TO and LO modes at temperatures above 440 °C, but was stable (i.e. only GaSb observed by RS) at lower temperatures. The critical temperatures for the other materials were: AlSb:As_4=440 °C, InSb:As_4=320 °C, GaAs:Sb_4=700 °C, InAs:Sb_4=540 °C, and AlAs:Sb_4>800 °C.

We investigated growth temperature limits in As/Sb heterostructures by growing a series of SLs in which every ninth monolayer of Sb was replaced by As or vice-versa. As an example, a growth sequence, repeated 40 times, was: (14 s GaSb, 3 s Sb, 2 s Ga, 7 s As, 2 s Ga) with a GaSb growth rate of 0.50 ML/s, yielding a nominal structure of: 40×(8 ML GaSb/1 ML GaAs)/1μm GaSb/GaAs(001)-substrate. SLs were grown at several different temperatures for each of the six cases (As MLs in GaSb, AlSb, or InSb and Sb MLs in GaAs, AlAs, or InAs) and characterized by x-ray diffraction. Selected samples were also characterized by Raman spectroscopy and cross-sectional TEM.[87]

Single-crystal x-ray diffraction data for the case of As_2 MLs in GaSb are shown in Fig. 9.19a. Growth temperatures of 400 and 420 °C produced structures with four satellite x-ray peaks, indicating a well-defined SL was present. The average lattice constants of the structures are consistent with coherently strained SLs and 1.0±0.2 ML GaAs per period. At a growth temperature of 450 °C, the n=0 and n=-1 satellites are present but substantially broader than at lower temperatures. For higher temperatures (480 and 520 °C), no satellites are observed. We attribute this to intermixing of As and Sb. An additional sample was grown at 480 °C using As_4 instead of As_2. The x-ray spectra is similar to the 450 °C As_2 sample, suggesting that the As_4 is less aggressive in attacking the GaSb surface. This is consistent with XPS and RHEED studies on InAs and GaSb surfaces. Wang *et al.*[88] and Collins *et al.*[89] investigated replacement of Sb on a GaSb surface during As_x irradiation. They found that As_2 replaced Sb much faster than As_4. Similarly, Sb_2 was more efficient than Sb_4 at replacing As on an InAs surface.

Results similar to Fig. 9.19a were obtained for As MLs in InSb (using As_2), but with a critical temperature of approximately 350 °C. Our critical temperatures for As MLs in InSb and GaSb are in reasonable agreement with the results of Yano *et al.*[85] For As MLs in AlSb, SL satellite peaks are observed over the entire temperature range investigated, 400–580 °C, although some degradation is apparent at temperatures above 500 °C.

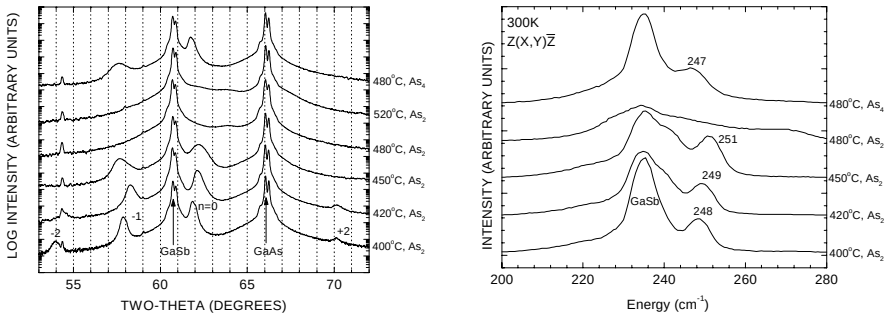

(a) (b)

Figure 9.19: (a) X-ray diffraction θ-2θ scans showing the (004) reflections for superlattices formed by inserting As monolayers into GaSb. All layers were grown on GaAs substrates with 1.0 μm GaSb buffer layers. Growth temperatures and As species are indicated. (b) Raman spectra for the samples of (a). Both GaSb longitudinal-optic modes (235 cm^{-1}) and GaAs planar vibrational modes (247–251 cm^{-1}) are observed. (Curves are offset for clarity.)

The vibrational properties of As MLs in GaSb were probed by Raman spectroscopy. Room-temperature spectra are shown in Fig. 9.19b. The optical phonon modes from the GaSb layers occur near 235 cm^{-1} for all five samples. In addition, clear evidence for a localized GaAs-like mode, known as a planar vibrational mode (PVM), is observed near 250 cm^{-1} for four of the samples. At a growth temperature of 400 °C, the GaSb mode is symmetric and the GaAs mode energy is 248 cm^{-1}. As the growth temperature is increased to 420 and 450 °C, the energy of the GaAs mode increases and additional scattering appears on the high-energy side of the GaSb peak. At 480 °C, there is no distinct GaAs peak although additional scattering is present near 270 cm^{-1}. These results are consistent with the x-ray diffraction data which showed the SL satellites broadening at 420 and 450 °C, and disappearing at 480 °C. The increase in energy of the GaAs mode with increasing growth temperature is consistent with the As being less confined to a single monolayer as the temperature is increased.[90,91,92] The resulting As contamination of the adjacent GaSb layers could explain the additional scattering near 240 cm^{-1}. The 480 °C sample with As_4 has a symmetric GaSb peak and a GaAs mode at an energy of 247 cm^{-1}. This data is consistent with incorporation of less than a ML of As.[93] The average As incorporation per period of the 480 °C-As_4 sample is 0.8 ML based upon x-ray diffraction measurements.

The results are quite different for Sb MLs in (In,Ga,Al)As. For Sb in GaAs, satellite peaks are observed from 330 °C to 600 °C, as shown in Fig. 9.20. For

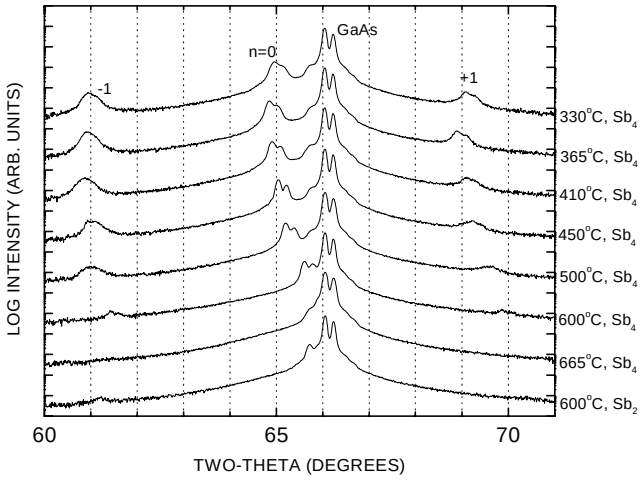

Figure 9.20: X-ray diffraction θ-2θ scans showing the (004) reflections for superlattices formed by inserting Sb monolayers into GaAs. All layers were grown on GaAs substrates. Growth temperatures and Sb species are indicated. (Curves are offset for clarity.)

T$\leq$450 °C, the average lattice constants of the SLs are consistent with coherent SLs and 1.0$\pm$0.1 ML GaSb per period. At higher temperatures, satellites are still present, but the amount of Sb incorporation decreases with increasing temperature. The results are summarized in Fig. 9.21 where we plot the number of Sb MLs incorporated per period as a function of growth temperature for all three materials. Sb MLs in InAs exhibit behavior similar to that of Sb in GaAs, but with a lower critical temperature ($\sim$410 °C). For Sb in AlAs, the critical temperature is approximately 480 °C, but only 0.8 ML Sb is incorporated at the lower temperatures. In all three cases, the results are consistent with Sb evaporation at higher temperatures. As expected, the critical temperature is lowest for InSb which also has the lowest congruent sublimation temperature ($\sim$400 °C). In contrast, the Yano *et al.* Raman measurements on arsenide layers subjected to an Sb_4 flux were not affected by evaporation but were sensitive to exchange reactions and the formation of compounds such as GaSb.[85] Hence, their observed critical temperatures were much higher.

9.3.3 Interface Bonds

Heterostructures formed from binary semiconductors that do not contain either a common anion or cation offer new flexibility in materials engineering. This flexibility arises because heterojunctions formed between AB and CD semicon-

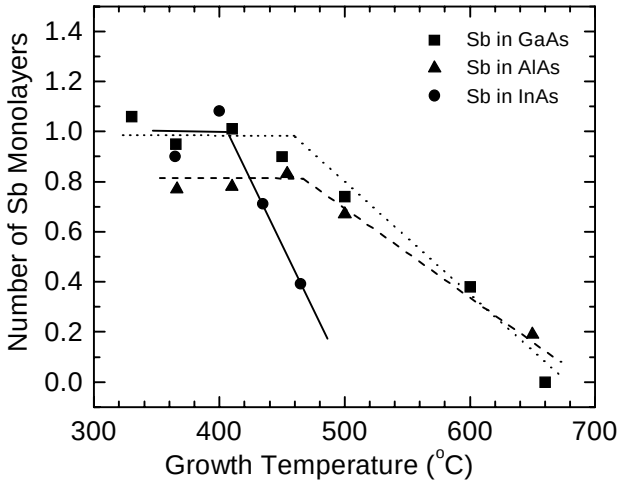

Figure 9.21: Number of monolayers of Sb incorporated per period for superlattices formed by inserting Sb monolayers into GaAs, AlAs, and InAs. As the growth temperature increases, less Sb is incorporated for each material.

ductors can, in principle, be bonded by either AD or BC bonds.[94] The cases of interest here are InAs/GaSb heterojunctions with InSb or GaAs interfaces and InAs/AlSb heterojunctions with InSb or AlAs interfaces. The latter case is illustrated in Fig. 9.22. Two MBE growth techniques have been applied to control interfacial composition. In one, migration enhanced epitaxy (MEE), cation and anion monolayers are alternately supplied to form the interface. For example, to form InSb-like bonds at InAs/GaSb interfaces, the shutter sequence is: InAs, 1 s In, 2 s Sb, GaSb, 2 s Sb, 1 s In, InAs, for an In growth rate of 1 ML/s. The other technique uses anion soaks at the interfaces. For the same example, the shutter sequence is: InAs, 5 s Sb, GaSb, 5 s Sb, InAs. We will demonstrate the control of interfaces and the impact of interfacial composition on material and device properties later in this section.

9.3.4 InAs/AlSb Superlattices

Superlattices composed of InAs and AlSb have been proposed as cladding material in diode lasers operating in the 2–5 μm spectral range [95] as well as barrier layers for InAs-channel field-effect transistors.[96] We will now use the example of InAs/AlSb superlattices to examine the role of growth temperature, lattice mismatch, and interfacial composition. In the first set of experiments,

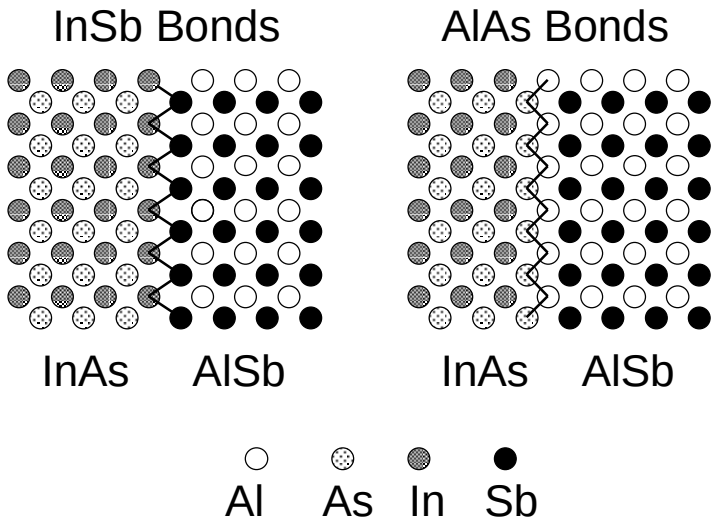

Figure 9.22: Interfacial bonding configuration for InSb-like and AlAs-like bonds at the InAs/AlSb interface as viewed along the [100] direction.

30-period SLs were grown with 4 ML InAs and 17 ML AlSb per period. MEE was used to form AlAs-like interface bonds. The buffer layer sequence was: 1.0 μm AlSb/1.0 μm GaSb/0.1 μm AlSb/0.3 μm GaAs/GaAs(001)-substrate. The AlSb and GaSb buffer layers were grown near 500 °C, and the SL growth temperature was varied. X-ray diffraction results for SL growth temperatures of 410, 450, and 480 °C are shown in Fig. 9.23.[97] Several satellite peaks (labelled 0, +1, -1, etc.) are visible for the 410 °C sample; some of the satellites exhibit Kα_1-Kα_2 splitting. At 450 °C, the satellite peaks are weaker, and the Kα_1-Kα_2 splitting is absent, indicating a degradation in SL quality. No satellites are observed at 480 °C. The results are consistent with PL measurements which show strong luminescence at 1.13 eV for the 410 °C sample. The PL intensity drops by a factor of 30 (200) at 450 °C (480 °C). RHEED patterns were monitored during growth of additional samples with the same structure. At 400 and 450 °C, the pattern was streaky with monolayer oscillations. At 490 °C, however, no oscillations were visible and a transmission spot pattern developed. We speculate that at high temperatures an As-Sb exchange reaction results in highly strained AlSbAs. The strain induces 3D growth, resulting in a degradation of structural and optical properties.

A second set of samples was grown with 40 periods of 10 ML InAs/10 ML AlSb.[98] The substrate temperature was fixed at 420 °C. Ideally, the lattice

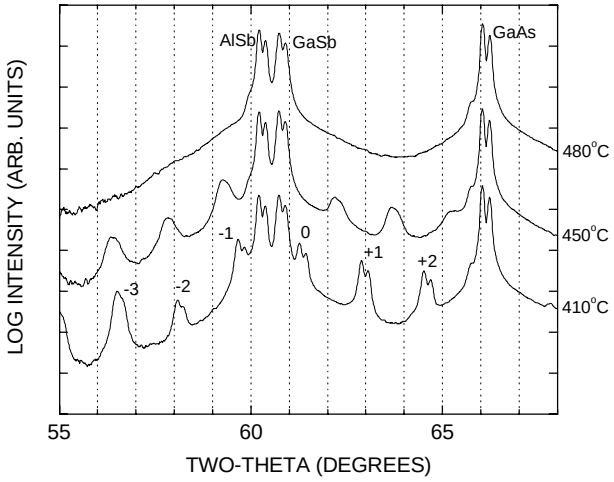

Figure 9.23: X-ray diffraction θ-2θ scans showing the (004) reflections for superlattices consisting of 30 periods of (4 ML InAs/17 ML AlSb) with AlAs-like interfacial bonds. At 480 °C, only the buffer layer and substrate peaks are visible, but superlattice satellites are present at lower growth temperatures. (Curves are offset for clarity; reproduced with permission from Ref. [97].)

constant of the buffer layer should be equal to the average lattice constant of the SL to avoid relaxation. The lattice constant of GaSb is halfway between those of AlSb and InAs and hence would seem to be the logical choice in this case. The presence of interface bonds with substantially different lattice constants (6.479 Å for InSb and 5.661 Å for AlAs), however, complicates the situation.

Superlattices with three different buffer layer sequences were investigated. One buffer layer consisted of 0.1 μm AlSb followed by 1.0 μm GaSb. XRD measurements show that the GaSb is almost fully relaxed. We refer to this buffer as GaSb. A second buffer was 1.0 μm of relaxed InAs. The third buffer was 0.5 μm InAs followed by 1.0 μm of relaxed AlSb. The InAs layer was included so that the temperature increase, resulting from growth of a small band-gap material on a large band-gap material,[83] would occur before the SL was grown. We refer to this buffer as AlSb.

In Fig. 9.24, we show the XRD results for SLs on all three buffer layers with InSb-like (a) and AlAs-like (b) interfaces. In each case, we observe several satellites from the SL as well as peaks due to the GaAs substrate and buffer layer(s). The position of the n=0 peak is related to the average lattice constant of the SL via Bragg's law. In some cases, Kα_1-Kα_2 splitting is visible. There

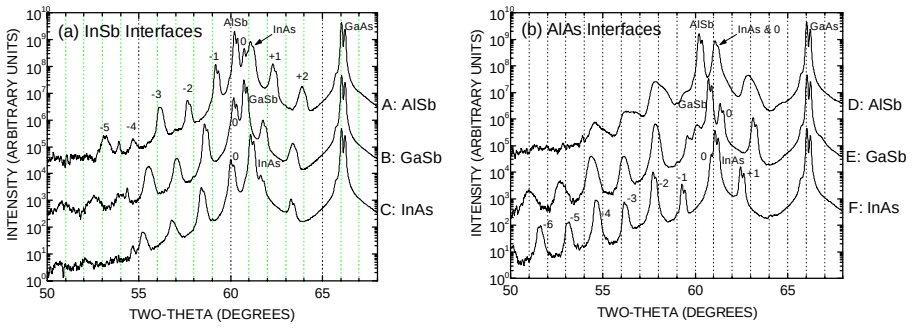

(a) (b)

Figure 9.24: X-ray diffraction θ-2θ scans showing the (004) reflections for superlattices consisting of 40 periods of (10 ML InAs/10 ML AlSb) with (a) InSb-like interfaces and (b) AlAs-like interfaces. The buffer layer for each sample is indicated. (Curves are offset for clarity; reproduced with permission from Ref. [98].)

is a clear variation of structural quality with buffer layer for the AlAs-bonded samples. Sample F (InAs buffer) is clearly the best; the average lattice constant of the SL is almost equal to that of the buffer. Sample D (AlSb buffer) has the largest mismatch and the SL quality is inferior, possibly due to the formation of misfit dislocations.

We compared our experimental XRD results to dynamical simulations which included the interfacial layers. For all SLs except sample D, the measured and predicted average lattice constants perpendicular to the growth direction agree to within 0.015 Å. This implies that the SLs are essentially coherent, with an in-plane lattice constant equal to that of the buffer layer. For sample D, the predicted perpendicular lattice constant is 6.015 Å and the experimental value is 6.057 Å, indicating a partial relaxation of this SL.

The Z(X,Y)$\overline{Z}$ RS spectra of the second set of InAs/AlSb SLs are shown in Fig. 9.25. For samples A–C (nominally InSb bonds), a single peak between 340 and 350 cm^{-1} is visible. It results from the confined longitudinal optic (LO) phonon modes for AlSb. We do not observe distinct energy splittings between the confined phonon modes of even index. This implies that the dispersion curve of the LO phonon in AlSb is rather flat. Samples E and F (nominally AlAs bonds) exhibit two peaks in this energy range. The lower energy peak for each is the AlSb LO. We attribute the higher energy peaks to the PVM involving stretching of the AlAs bonds. The absence of this mode in our SLs with nominally InSb-like bonds indicates good interfacial control.

We note the small differences in energy for the AlSb LO phonon modes

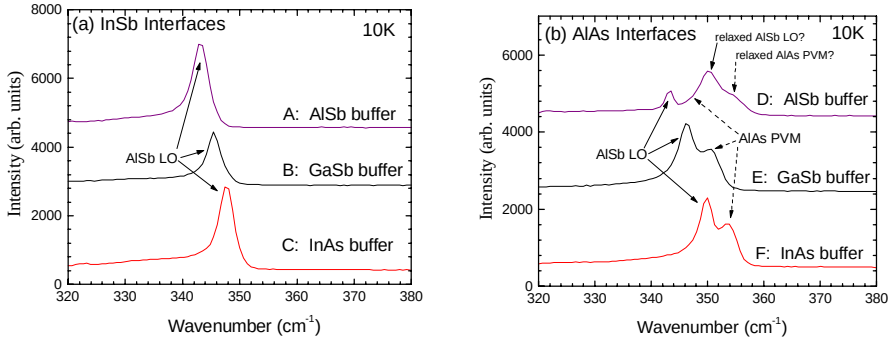

(a) (b)

Figure 9.25: Raman scattering data at 10 K with the Z(X,X)$\overline{Z}$ geometry for the samples of Fig. 9.24. The confined AlSb LO mode is present for all samples. An AlAs planar vibrational mode is identified for samples with AlAs-like interfaces. (Curves are offset for clarity; reproduced with permission from Ref. [98].)

in Fig. 9.25. The differences can be qualitatively explained by biaxial strain in the AlSb layers of the SL, with the largest strain for InAs buffer layers and the smallest for AlSb buffer layers. The shift of the AlAs PVM from sample E to F also results from strain. For sample D, we speculate that the upper portion of the SL is partially relaxed and the lower portion is coherent. Such a structure could result in the observed Raman features as well as the broadened XRD satellites.

9.3.5 InAs/AlSb Single Quantum Wells for High-Frequency Field-Effect Transistors

Single quantum wells of InAs clad by AlSb are of interest for applications that require low-voltage, high-speed field-effect transistors. Advantages of this materials system include the high electron mobility (30,000 cm^2/V-s) and velocity (4×10^7 cm/s) of InAs,[99] and a large conduction band offset between InAs and AlSb (1.35 eV).[100] Disadvantages include impact ionization due to the small band gap of InAs,[101] and processing problems associated with the high reactivity of AlSb.

The group of Prof. Kroemer at University of California at Santa Barbara (UCSB) reported high-mobility InAs/AlSb SQWs in 1989, with room-temperature and low-temperature mobilities as high as 28,000 and 330,000 cm^2/V-s, respectively.[102] They found that high mobilities could be achieved if

and only if the lower interface were composed of InSb-like rather than AlAs-like bonds.[103] The UCSB group also examined the well-width dependence of transport properties. Highest mobilities were obtained for InAs thicknesses of 130–200 Å. Reduced mobilities for thinner wells were attributed to interface roughness scattering.[104] Thicker wells presumably exceeded the critical layer thickness, resulting in the formation of misfit dislocations and a reduction in mobility.[105] More recently, low-temperature mobilities of 6–9$\times 10^5$ cm^2/V-s have been achieved with 1.4–2.0 μm GaSb buffer layers.[106,107]

Sheet carrier concentrations for unintentionally doped InAs/AlSb SQWs are typically 0.4–1.0$\times 10^{12}$/cm^2. Densities can be increased to 1.5–2.0$\times 10^{12}$/cm^2 by an As-soak technique.[103,108] In this procedure, a layer of AlSb, typically 100 Å, is grown above the InAs QW and terminated with a monolayer of Al. The surface is soaked in a beam of As_2 for 10–60 s at 500 °C. Then, additional AlSb and an InAs cap are grown. The origin of the donors is not clear but could result from As_{Al} antisite defects.

Higher sheet charge densities are desirable for FET applications. Si is the most common n-type dopant in III-V MBE systems. Si is, however, amphoteric in the III-V's, producing n-type GaAs, InAs, AlAs, and InSb, but p-type GaSb and AlSb. Chalcogens such as Te have been used as an n-type dopant in AlSb, resulting in sheet carrier concentrations as high as 3.8$\times 10^{12}$/cm^2 in InAs/AlSb FETs.[109] A disadvantage of introducing Te into an MBE system is its high vapor pressure and the resulting memory effects. An alternative to chalcogen doping of GaSb and AlSb is modulation doping using a thin Si-doped InAs layer adjacent to the channel. Malik *et al.* applied this technique to InAs/GaSb SQWs and achieved densities as high as 3.6$\times 10^{12}$/cm^2.[110] Bolognesi *et al.* used InAs/AlSb SLs as barriers for an InAs quantum well and doped selected InAs layers with Si to obtain a sheet carrier density of 1.3$\times 10^{12}$/cm^2.[96]

In order to achieve doping of the InAs quantum wells, we designed a structure in which a 4 ML (12 Å) layer of Si-doped InAs is inserted 125 Å above the 50 ML InAs well (Fig. 9.26). The large confinement energy of the 4 ML quantum well allows the electrons to transfer into the 50 ML InAs channel. The challenge in this approach was to develop a procedure to avoid segregation of Si atoms into the AlSb and the resulting self-compensation of the Si donors in the InAs. Hall effect measurements were performed on narrow Si-doped InAs quantum wells grown under a variety of conditions. At the normal growth temperature of 500 °C more than 50% of the Si atoms segregate out of the 4 ML InAs layer and n-type conductivity is not obtained. We achieved n-type conductivity by lowering the growth temperature to 370–420 °C during growth of the 4 ML InAs(Si) layer. Results are shown in Fig. 9.27 where we plot sheet carrier concentration and room temperature mobility versus Si

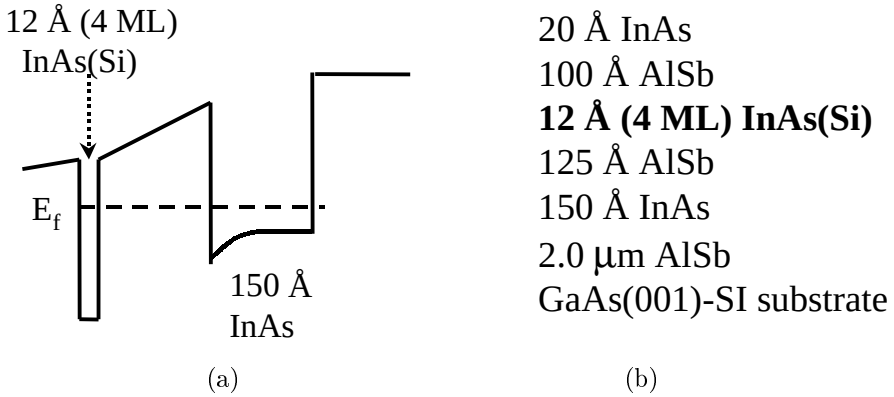

Figure 9.26: (a) Schematic of band structure and (b) heterostructure cross-section for modulation InAs(Si) doping of InAs/AlSb quantum wells.

cell temperature. For the first three samples, carrier concentrations range from 1.7–2.6×10^{12}/cm^2 with mobilities of 23,000–25,000 cm^2/V-s. The fourth sample has a sheet carrier concentration of 3.2×10^{12}/cm^2 and a mobility of 16,000 cm^2/V-s. Quantum Hall-effect measurements show no evidence of a parallel conduction channel in the Si-doped InAs layers for these four samples. (A parallel channel was observed for a sample with higher doping density.) Only a single sub-band is occupied for the first three samples. A second sub-band is occupied for the 3.2×10^{12}/cm^2 sample, causing the reduction in mobility.[111] Recent independent work by Sasa *et al.* achieved sheet carrier concentrations in the 2–4×10^{12}/cm^2 range by Si planar doping of a 6 ML InAs quantum well located 80 Å below a 150 Å InAs quantum well clad by AlGaSb.[112]

Considerable progress in the device performance of InAs/AlSb FETs was reported in the early 1990's, with gate lengths in the 0.5–2.0 μm range.[109,113,114,115] This system appears promising for low-power, low-noise applications. Recently, gate lengths have been reduced to 0.1–0.2 μm.[108,116,117] In addition, we have included an InAlAs/AlSb composite upper barrier and p^+GaSb layer within the AlSb buffer. The complete heterostructure. (from cap to substrate) is:

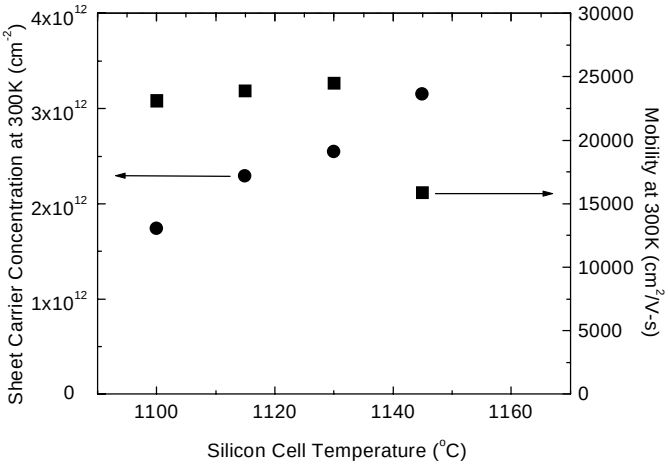

Figure 9.27: Room-temperature sheet carrier density and mobility as a function of silicon cell temperature for 50 ML InAs/AlSb quantum wells modulation doped by 4 ML InAs(Si) layers. The InAs(Si) layers were grown at 380 °C. (Reproduced with permission from Ref. [111].)

15 Å	InAs
40 Å	$In_{0.4}Al_{0.6}As$
As soak	
125 Å	AlSb
100–150 Å	InAs
500 Å	AlSb
200 Å	p^+GaSb
2.4 μm	AlSb
SI GaAs substrate	

The InAlAs and p^+GaSb layers eliminated the anomalous kink-effect typically seen in the I-V characteristics of InAs/AlSb FETs and reduced the leakage current. The resulting device characteristics for a 0.1 μm gate length include a transconductance of 600 mS/mm and an extrinsic unity current gain cut-off frequency, f_T, of 160 GHz at a source-drain voltage of 0.45 V. FETs with a 0.5 μm gate length exhibit a transconductance of 1 S/mm and an intrinsic f_T-L_g product of 50 GHz-μm.[118] This f_T-L_g product is equal to the highest that has ever been achieved in any material system at this gate length.

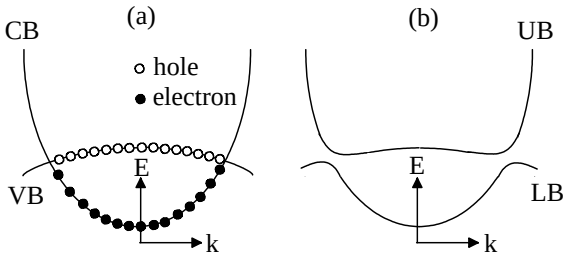

Figure 9.28: (a) Relative band alignment of the conduction band of InAs (CB) and the heavy-hole valence band of GaSb (VB). (b) Hybridized band structure of the InAs/GaSb with a lower band (LB) completely filled with electrons and an upper band (UB) completely empty.

9.3.6 InAs/GaSb Single Quantum Wells

Since the pioneering work of IBM [119,120] in the late 1970's, InAs/GaSb heterostructures have served as the archetypal system to explore the impact of a type-II band alignment on the properties of quantum wells and superlattices. Shown in Fig. 9.28a is the relative band alignment of the conduction band of InAs (CB) with the heavy-hole valence band of GaSb (VB). While the theoretically or experimentally determined values for the band alignment are still somewhat uncertain, the energy difference between CB and VB at k=0 and without quantum confinement is accepted to be about 150 meV.[121,122] Part of the uncertainty arises because this value is a function of biaxial strain in the materials as well as the interface bond type.[123,124,125,126,127,128] Because the valence band of GaSb occurs at higher energy than the conduction band of InAs, one expects the formation of an InAs/GaSb heterojunction will induce the flow of electrons from the valence band of GaSb into the empty states in the conduction band of InAs. The first experiments performed in this system focused on the creation of this new type of semimetal characterized by a spatial separation of free electrons in the InAs from the free holes in the GaSb with, as shown in Fig. 9.28a, both the electrons and holes occupying the same values of k-space. This is to be contrasted with a conventional semimetal where the electrons and holes coexist in the same regions of real space but occupy different regions of k-space.

Although many workers in the nanostructure field continue to ascribe the formation of a new class of intrinsic semimetal to the InAs/GaSb system, Altarelli and co-workers pointed out that this viewpoint is not compatible with the symmetry of the bulk band structures of InAs and GaSb.[121,129,130,131]

Specifically, they showed that a $k*p$ interaction between the CB of InAs and the VB of GaSb results in a breakdown of the simple semimetal viewpoint. As denoted in Fig. 9.28b, this interaction causes a level crossing and induces the formation of a small energy gap. There are no free carriers at low temperatures because the lower band (LB) is completely filled with electrons and upper band (UB) is completely empty. However, there has still been a net charge transfer of electrons from GaSb into InAs. This charge transfer is evident in the character of the wavefunction as a function of k in the LB. Specifically, for the LB at k=0 the wavefunction is mainly localized in InAs. This state was initially empty before the electrons moved from the valence band of GaSb into the InAs. Near the crossing point of the unperturbed CB and VB, the wavefunction is delocalized in both InAs and GaSb. As k increases the admixture of GaSb wavefunction continues to increase until at large k the wavefunction of the LB is mainly localized in the GaSb. In a similar way the wavefunction in the UB is of mixed character, where at k=0 the wavefunction is mainly localized in the GaSb. After the heterojunction forms, the initially-filled valence band is empty. Accurate band-structure calculations require this real space transfer of charge to be modeled with self-consistent Hartree theory. This is not required if the layer thicknesses of InAs and GaSb are made small enough that the sum of confinement energies of the k=0 LB and UB is larger than that the energy difference between the VB of GaSb and the CB of InAs. Fortunately, this is the case for the layer thicknesses required in infrared detector and laser applications. However, for all cases the strong band interactions between the conduction band states of InAs and the valence band states of GaSb require the application of a multi-band $k*p$ envelope function approximation.

While the initial experimental data appeared to be explained with the semimetallic model illustrated in Fig. 9.28a, Altarelli and co-workers elucidated how the hybridized model in Fig. 9.28b could also explain the data.[121,129,130,131] They noted that all of the observed properties in this system could be accounted for in the context of the hybridized model shown in Fig. 9.28b if the carriers arose from an extrinsic doping process. Because the early work indicated that the electron and hole densities were not equal, it was clear that extrinsic doping was contributing to the observed carrier densities. In the case of extrinsic doping, the chemical potential, μ, at T=0 lies in either the valence or conduction band. If μ lies above (below) the k=0 energy of the UB (LB) only electrons (holes) are observed. Shown in Fig. 9.29 is a schematic representation of the case when μ lies in the highly nonparabolic region of the conduction band. Near k=0 there is a pocket of holes and, at larger k, a donut of filled electron states. In extrinsically doped samples with μ in this location, both electrons and holes are observed in cyclotron resonance (CR) and Hall

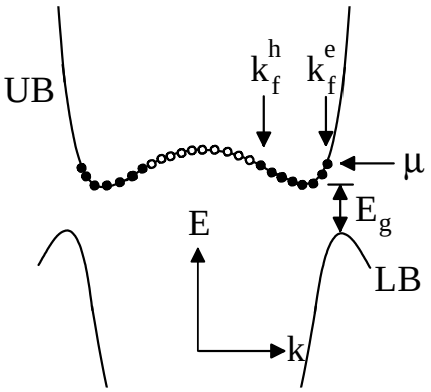

Figure 9.29: Schematic representation of InAs/GaSb band structure for the case when the chemical potential, μ, lies in the highly nonparabolic region of the conduction band.

effect measurements. The locations of the Fermi wavevector of electrons and holes determine the quantitative properties. Treating the Hall effect with a two-carrier analysis, the density of holes or electrons is given by,

$$N_S^{e,h} = \frac{(k_f^{e,h})^2}{2\pi} \tag{9.1}$$

where $k_f^{e,h}$ is the electron or hole Fermi wavevector and $N_S^{e,h}$ is the 2D electron or hole density. The total number of electrons in the upper band is given by,

$$N_T = N_S^e - N_S^h = \frac{(k_f^e)^2}{2\pi} - \frac{(k_f^h)^2}{2\pi} \tag{9.2}$$

In a nearly intrinsic sample, $N_T \to 0$ and $k_f^e \cong k_f^h$ implying that the upper band is nearly empty. Recently, Daly and co-workers have reported samples with $N_T \to 0$.[132] Because both electrons and holes were observed in the early CR and Hall effect measurements, these experiments were thought to verify the semimetallic model in Fig. 9.28a. However, this observation is compatible with the hybridized band structure of Fig. 9.29 where μ lies in either the UB or LB.

Recent CR measurements have shown the importance of the electron-hole hybridization. When the carriers exist in a parabolic band, the energy of conventional CR is given by,

$$\hbar\omega_{CR} = \frac{eB}{m^* c} \tag{9.3}$$

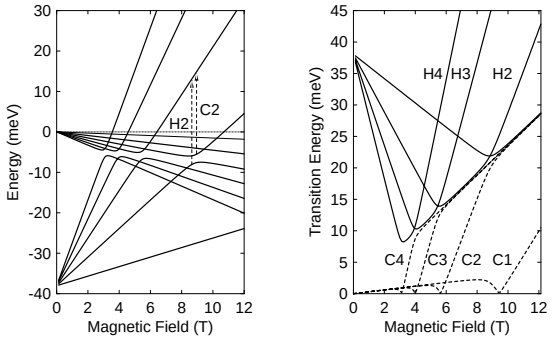

(a) (b)

Figure 9.30: Calculated results for an InAs/GaSb electron-hole hybridized two-band model where the subband gap is 38 meV, the hybridized gap is 2 meV, electron effective mass is $0.049m_o$, and hole effective mass is $0.38m_o$. (a) The Landau level development. (b) The C and H transitions. (Reproduced with permission from Ref. [125].)

This simple expression does not apply to the highly nonparabolic band structure shown in Fig. 9.29. As indicated by Altarelli and reproduced by Wagner *et al.*[125] and Kono *et al.*[133] in the most recent CR data, CR exhibits a very different and complex frequency dependence. Shown in Fig. 9.30a are energies of the Landau levels (LL) calculated from a two-band model including band hybridization. The arrows in the figure denote potentially allowed CR (C2) and interband (H2) transitions. In Fig. 9.30b, the energies of CR are denoted by Cn and the interband transitions by Hn where n is a label that denotes the LL indices involved in the transition. The observation of these transitions requires that the low-energy LL is partially filled and the upper LL is partially empty. The rapid change in Cn transitions at low energies has been observed by all of the CR studies that have been performed over the past 15 years. In the earliest work these transitions were ascribed to interband transitions and not CR. While the low temperature CR measurements of Wagner *et al.* indicate no evidence of conventional CR described by Eqn. 9.3, at higher temperatures conventional CR is observed.[125] This peculiar observation is characteristic of the hybridized band structure. Specifically, because at low temperatures and low electron densities the carriers exist in the highly nonparabolic region of the band structure, conventional CR is not expected to be observed. However, at higher temperatures, the carriers are thermally excited into regions of the band structure that are fairly parabolic and normal CR behavior is observed.

Further support for the hybridized viewpoint comes from the data of Kono

et al. that show the smooth merging of the Cn transitions with the energy of conventional CR.[133] A careful examination of Fig. 9.30a indicates that this behavior is observed when μ is not located at the bottom LL. Higher LL's need to be occupied to observe CR energies consistent with Eqn. 9.3. This can happen by heating the sample to higher temperatures, as observed by Wagner *et al.*, or by looking at more heavily doped samples. While many aspects of the CR model of Fig. 9.30b have been reported, the Hn transitions do not exhibit characteristics in total agreement with this predicted behavior. Specifically, while the earliest magneto-optical work and the more recent work of Wagner *et al.*, reveal Hn transitions with positive slopes, the predicted interband transitions with negative slopes have not been reported. These transitions are expected to be more difficult to observe because they can become partially or totally blocked by occupancy of the lowest UB LL by electrons.

Kono and co-workers also observe new magneto-optical transitions not predicted by the hybridized model. This observation led them to propose the formation of a bound electron-hole state induced by the excitonic interaction. The new magneto-optical features are attributed to the internal transitions of excitons. The NRL group has observed similar "bound state" features in asymmetric InAs/GaSb quantum wells with GaAs interface bonds.[134] These features are missing in the asymmetric samples with InSb interface bonds or in symmetric samples with either bond type. Recent theoretical work suggests that the "bound state" feature may arise from spin-splitting of the InAs conduction band.[135] Additional work is required to clarify these results.

Although the CR and transport studies exhibit evidence of the formation of a highly non-parabolic band structure, none of the studies has shown compelling evidence for the formation of the hybridization-induced energy gap. Recent capacitance, Hall effect, and transfer characteristics of Yang *et al.* exhibit characteristics consistent with the formation of a small band gap semiconductor.[136] In addition, by an examination of the three terminal transfer measurements as a function of in-plane magnetic field, the transition from a small band gap semiconductor to a true semimetal has been observed. This transformation is in agreement with the expected behavior of the hybridized band structure as a function of in-plane magnetic field.[136,137]

While there has been significant progress in understanding the band structure in this novel system, some questions remain and more work needs to be performed. In particular, issues related to exciton formation and the impact of interface bond type on hybridization need to be clarified. It is also possible that disorder at the interfaces can cause violation of wavevector conservation and complicate the simple hybridized viewpoint. However, with more work it may be possible to tune the hybridization gap and induce the formation of an

excitonic insulator. This interesting possibility has recently attracted theoretical attention because one can envision the formation of an excitonic insulator when the binding energy of the exciton is larger than the energy gap induced by hybridization. Under such circumstances, the comparison between the observed and predicted behavior of excitonic insulators could result in important contributions to our understanding of electron-electron interactions and offers the potential to study Bose condensation in a novel excitonic insulator system.

9.3.7 InAs/GaSb Superlattices for Infrared Detectors

As first proposed by Smith and Mailhiot,[138] strained-layer superlattices composed of InAs/(In)GaSb layers are a promising alternative to the HgCdTe system for use in infrared detectors. (Detailed discussions on infrared applications using II-VI and IV-VI materials can be found in Ref. [139] and Ch. 13 in this volume.) The band structure in this system is type-II, with a tunable energy gap. Hence, thin layers (7–16 ML) are required to achieve significant overlap of the electron and hole wavefunctions and high absorption coefficients. As a result, interfacial layers will be a significant fraction of the entire SL and are expected to influence the structural and optical properties.

To test interfacial control in this system, we grew 40-period superlattices with 8 ML InAs and 12 ML GaSb per period (designated as 8-12), as well as 8-8 and 12-8.[140] The nominal interface type was varied by using MEE. The growth temperature was chosen to be 400 °C based upon previous x-ray diffraction studies.[141,142] We show the XRD data for three samples with the 8-8 structure in Fig. 9.31a. Samples A and B were grown with all interfaces nominally InSb- and GaAs-like, respectively. For sample C, InAs was grown on GaSb with GaAs-like bonds and GaSb was grown on InAs with InSb-like bonds. For each sample, several SL diffraction peaks are observed in addition to the GaAs substrate and GaSb buffer peaks. The resolution of the Kα_1 and Kα_2 peaks for n=+1, 0, -1, and -2, along with the presence of higher order SL peaks, demonstrates reasonable crystalline quality for the SL's. As expected from Bragg's law, the n=0 peak for sample B (GaAs bonds) is at a larger angle than for sample A (InSb bonds). Sample C is at an intermediate value.

In Fig. 9.31b, we plot our experimental average lattice constants as a function of the theoretical values. The point labeled "8-8 InSb/GaAs" corresponds to curve C in Fig. 9.31a. The interfaces are reversed for the sample labeled "8-8 GaAs/InSb". The lattice constant differences due to interface bonds are largest for the 8-8 structures because the interfaces are a larger fraction of the total structure. In all cases, the theoretical predictions and experimental data agree to within 0.007 Å.

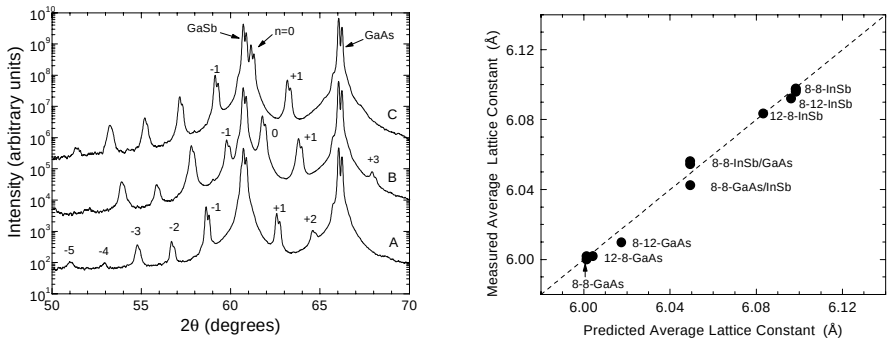

(a) (b)

Figure 9.31: (a) X-ray diffraction θ-2θ scans for three 40-period superlattices. Each period consists of 8 ML InAs and 8 ML GaSb, along with two interfaces (see text). Superlattice satellite peaks, as well as the GaSb buffer layer and GaAs substrate peaks, are visible. The curves are offset for clarity. (b) Measured versus predicted average lattice constant for InAs/GaSb superlattices. The number of MLs of InAs, number of MLs of GaSb, and nominal interface type are indicated for each sample. (Reproduced with permission from Ref. [139].)

Vibrational properties of GaSb/InAs superlattices have been investigated by several groups. Fasolino and co-workers predicted the existence of localized GaAs interface vibrations (or planar vibrational modes, PVMs) for structures with GaAs-like interfacial bonds.[94] Several groups have experimentally observed GaAs PVMs near 250 cm^{-1}. Raman scattering spectra from our superlattices show quasi-confined optical phonon modes from the GaSb and InAs layers near 236 cm^{-1}. In addition, clear evidence for the GaAs PVMs is observed near 253 cm^{-1}. In contrast, samples that are grown with InSb interfaces do not reveal this mode to within our signal to noise. Therefore, in agreement with the XRD measurements, the vibrational properties indicate that it is possible to control the chemical composition of the interfaces.

In other measurements [143,144] GaAs interface vibrational modes occurred at somewhat lower energies than what we observe. In order to understand this latter observation, samples with a mixed interface were grown intentionally.[93] The interfacial composition was determined by x-ray diffraction measurements. The Raman results (Fig. 9.32) show that the GaAs PVM shifts to lower energy if the plane of As atoms that bonds the GaSb and InAs layers is intentionally contaminated with Sb. This observation indicates that the energy of this mode is useful for quantifying the amount of contamination at the interface. For example, we grew an 8-8 SL using the Sb soak technique at the interfaces. The energy of the PVM indicated a mixed interface; we estimate approximately

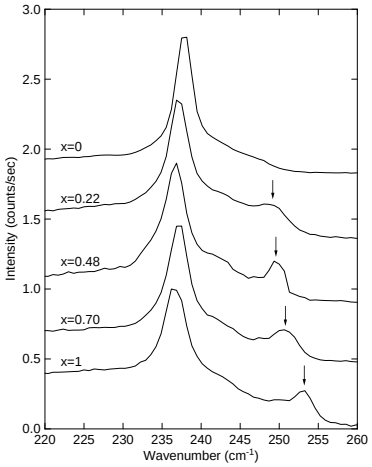

Figure 9.32: Raman scattering data at 10 K with the Z(X,Y)$\overline{Z}$ geometry for InAs/GaSb superlattices as a function of the As_xSb_{1-x} plane that connects the InAs and GaSb layers. The arrows denote the positions of the GaAs-like planar vibrational mode. The curves are offset for clarity. (Reproduced with permission from Ref. [93].)

15% GaAs-like bonds and 85% InSb-like bonds.[145] These results suggest that the MEE technique is superior to the Sb soak technique for achieving pure InSb-like interface bonds. We note that these experiments used Sb_4; results could be different for Sb_2.

An important addition to the type of information that can be obtained from Raman spectra was reported by Lyapin and co-workers.[146] They showed that under particular polarization conditions the vibrational properties of the top and bottom interfaces can be studied independently. Using this technique, Lyapin *et al.* determined the metalorganic chemical vapor deposition (MOCVD) growth sequences that resulted in abrupt GaAs- or InSb-like interfaces.

The interfaces in InAs/(In)GaSb superlattices have been imaged by cross-sectional, high-resolution TEM[147,148,149,150] and cross-sectional STM.[151,152,153] We will briefly review the highlights here; the reader is referred to the original papers as well as the recent book chapter by Twigg *et al.*[145] for additional details.

Using TEM, Twigg and co-workers found that the interface roughness was a function of bond type and strain for samples grown using MEE at the interfaces. The interface roughness for InAs/GaSb interfaces with InSb-like bonds grown on a GaSb buffer layer (InAs layer in tension) was approximately

1 ML. The interface roughness increased to 2–3 ML when the bond type was changed to GaAs-like and/or the buffer layer was changed to InAs (GaSb layer in compression). Plan-view STM studies of InAs/GaSb surfaces support these findings.[154] These results, along with the x-ray and Raman spectroscopy measurements discussed earlier, lead to the conclusion that the roughness associated with growth is the primary source of interfacial disorder, with intermixing playing a secondary role in the MBE/MEE-grown samples.

Feenstra *et al.* examined InAs/GaSb superlattices grown by MBE but using As and Sb soaks at the interfaces. Using cross-sectional STM, they observed evidence of exchange reactions at the interfaces, with more intermixing for the InAs-on-GaSb interface than the GaSb-on-InAs interface.[151] These findings were attributed to an antimony-terminated surface having a lower free energy than an arsenic-terminated surface. The result would be an exchange of Sb and As when InAs is grown on GaSb. Lew *et al.* investigated InAs/InGaSb superlattices with cross-sectional STM. They observed an anisotropy in interface structure, with interfaces in the $(1\bar{1}0)$ plane exhibiting a higher degree of interface roughness than those in the (110) plane.[153] In contrast to the results of Feenstra *et al.*, Lew and co-workers found that $In_{0.25}Ga_{0.75}Sb$-on-InAs interfaces are rougher than InAs-on-$In_{0.25}Ga_{0.75}Sb$ interfaces. Their samples were also grown with an Sb soak to form nominally InSb-like interfaces, but included $In_{0.25}Ga_{0.75}Sb$ rather than GaSb layers. The interfacial bond type affects not only structural and vibrational properties of InAs/GaSb SLs (also see Refs. 154 and 155) but also the electo-optical properties. Photoconductivity measurements of Waterman *et al.*[123] and Bennett *et al.*[157] showed that the band gap of SLs with InSb bonds was 20–50 meV smaller than similar SLs with GaAs bonds. Chow *et al.* used variable-temperature transport measurements to determine the band gap of InAs/InGaSb SLs and found a 25 meV difference, with a larger value for GaAs bonds.[158] Meyer *et al.* determined the InAs/GaSb valence band offset by magneto-transport and magneto-optical measurements. They found that the offset increased by 14 ± 5 meV when the bond type changed from GaAs-like to InSb-like.[126] In contrast, Wang *et al.* found the band offset to be independent of interface composition but a strong function of the growth order, with the InAs-on-GaSb interface exhibiting a larger valence band offset.[127] Other groups have also found that infrared reflectivity is a strong function of interface bond type.[155,159]

At least four groups fabricated infrared detectors based upon InAs/(In)GaSb SLs in the last five years.[160,161,162,163,164,165] Yang and Bennett applied a Schottky-diode-like structure in which the SL was grown on an n^+InAs buffer on a GaAs(SI) substrate.[160] A built-in field is established in the SL as a result of the Fermi level difference between the InAs buffer and the SL surface. The

device has a turn-on wavelength of 8 μm, and a responsivity of 0.07 A/W. The detectivity is relatively low, presumably as a result of large leakage currents. The dislocations generated by the 7% lattice mismatch between the InAs and GaAs are likely the dominant cause of the leakage currents.[160]

Research by Jack *et al.*[162] and Johnson *et al.*[163] investigated homojunction p-i-n InAs/InGaSb SL structures and heterojunction structures in which an unintentionally doped InAs/InGaSb SL region was sandwiched by doped InAs and/or GaSb layers. Both structures were grown on GaSb substrates to avoid generation of misfit dislocations. Detectivities of 1–2$\times 10^{10}$cmHz$^{1/2}$/W were achieved at 77 K for both types of devices at wavelengths of 7–10 μm.

The best detector characteristics reported to date are from the recent work of Fuchs *et al.* at the Fraunhofer Institute.[164,165] They used MBE to fabricate InAs/InGaSb homojunction p-i-n detectors. The complete structure is:

100 Å InAs(Si)
50×(12 ML InAs(Si)/10 ML $In_{0.2}Ga_{0.8}Sb$)
15×(12 ML InAs/10 ML $In_{0.2}Ga_{0.8}Sb$)
88×(12 ML InAs/10 ML $In_{0.2}Ga_{0.8}Sb$(Be))
5000 Å GaSb(Be)
GaSb(001)

The Si doping level in the n-type SL was 1×10^{18}/cm^3; the Be doping level in the p-type SL varied from 2×10^{17}/cm^3 to 1×10^{18}/cm^3 . The interface bond types alternated, with InSb-like interfaces for InAs on InGaSb and GaAs-like interfaces for InGaSb on InAs. In Fig. 9.33, we show the Fuchs *et al.* data for 8 μm photodiodes with a current responsitivity of 2 A/W (up to 180 K). The product of the dynamic impedance and the area, R_oA, along with the detectivity, D*, are plotted as a function of temperature. At 77 K, $R_oA\approx$1000 Ω-cm^2 and D*$\approx 10^{12}$cmHz$^{1/2}$/W are observed.

9.4 Summary

In recent years, researchers have reported significant advances in the growth of Sb-based semiconductors by MBE. An important factor has been the development of techniques to measure growth temperature and to characterize and control interfacial bonding. In addition, progress can be attributed to the availability of better source materials, high-quality GaSb substrates, and valved arsenic crackers.

The large lattice mismatch between InSb, GaSb, or AlSb and GaAs can lead to the formation of self-assembled quantum dots during the initial stages

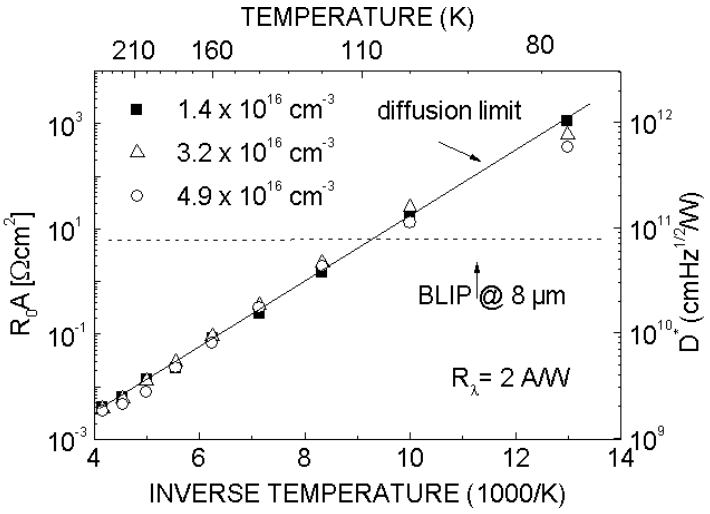

Figure 9.33: Temperature dependence of the dynamic impedance and detectivity at zero bias voltage for InAs/InGaSb superlattice p-i-n photodiodes. (Reproduced with permission from Ref. [164].)

of epitaxy. As discussed in Sec. 9.2.2, these QDs have a type-II band alignment with holes in the (In,Ga,Al)Sb and electrons in the surrounding GaAs. Raman spectra reveal vibrational modes that are sensitive to the composition of the QDs. *In situ* STM experiments reveal a complex wetting layer structure.

Lattice mismatches are small, but not negligible, within the 6.1 Å family of InAs, GaSb, and AlSb. The unique band alignments of these materials have led to proposals for several electronic and electro-optic devices. As discussed in Sec. 9.3, progress has been reported for both high-frequency FETs and infrared detectors. In addition, several groups have recently advanced the state-of-the-art in infrared lasers and resonant tunneling diodes based upon arsenide/antimonide heterostructures. In the future, work on fundamental issues of band structure and epitaxial growth should continue in parallel with device development. At this point, we are only beginning to explore the connections between electronic/optical properties and morphology, surface reconstructions, interfacial abruptness, and anion species.

Acknowledgments The authors thank our colleagues at NRL for their important contributions to the research described here. They include: J.B. Boos, J.L. Davis, H.B. Dietrich, M. Fatemi, E.R. Glaser, M. Goldenberg, L.A.

Hemstreet, W. Kruppa, R. Magno, W.J. Moore, D. Park, P.M. Thibado, M.E. Twigg, R.J. Wagner, J.R. Waterman, M. Weimer, L.J. Whitman, and M.J. Yang. We also thank J.C. Ferrer, F. Fuchs, and F. Hatami for permission to include their data, and W.K. Liu, M.B. Santos, and J. Venables for a critical reading of the manuscript. The Office of Naval Research supported this work.

References

1. C.-A. Chang, R. Ludeke, L.L. Chang, and L. Esaki, *Appl. Phys. Lett.* **31**, 759 (1977).
2. R. Ludeke, *IBM J. Res. Develop.* **22**, 304 (1978).
3. M. Yano, Y. Suzuki, T. Ishii, Y. Matsushima, and M. Kimata, *Jpn. J. Appl. Phys.* **17**, 2091 (1978).
4. G.M. Williams, C.R. Whitehouse, C.F. McConville, A.G. Cullis, T. Ashley, S.J. Courtney, and C.T. Elliott, *Appl. Phys. Lett.* **53**, 1189 (1988).
5. J.L. Davis and P.E. Thompson, *Appl. Phys. Lett.* **54**, 2235 (1989).
6. For example, see W.K. Liu, X. Zhang, W. Ma, J. Winesett, and M.B. Santos, *J. Vac. Sci. Technol. B*, **14**, 2339 (1996).
7. For example, see T. Ashley, C.T. Elliott, R. Jefferies, A.D. Johnson, G.J. Pryce, A.M. White, and M. Carroll, *Appl. Phys. Lett.* **70**, 931 (1997).
8. For example, see I.J. Fritz, L.R. Dawson, J.A. Olsen, and A.J. Howard, *Appl. Phys. Lett.* **67**, 2320 (1995).
9. For example, see D.H. Chow *et al.*, *IEEE Electr. Dev. Lett.* **17**, 69 (1996).
10. For reviews, see chapters in *Antimonide Related Strained-Layer Heterostructures*, ed. M. O. Manasreh (Gordon and Breach, Amsterdam, 1997): J.R. Meyer, J. I. Malin, I. Vurgaftman, C.A. Hoffman, and L.R. Ram-Mohan, 235–272; G.G. Zegrya, 273–368; G.W. Turner and H.K. Choi, 369–432; R.H. Miles and T.C. Hasenberg, 433–460; Y.-H. Zhang, 461–500.
11. For a review, see R.A. Stradling, *Braz. J. Phys.* **26**, 7 (1996).
12. For example, see G.R. Booker *et al.*, *J. Cryst. Growth*, **146**, 495 (1995); R.M. Biefeld, A.A. Allerman, and S.R. Kurtz, *J. Cryst. Growth*, **174**, 593 (1997); and C.A. Wang, *J. Cryst. Growth*, **170**, 725 (1997)
13. J.M. Kang, M. Nouaoura, L. Lassabatere, and A. Rocher, *J. Cryst. Growth*, **143**, 115 (1994).
14. R.N. Kyutt *et al.*, *Phys. Solid State*, **35**, 372 (1993).
15. P.M. Thibado, B.R. Bennett, M.E. Twigg, B.V. Shanabrook, and L.J. Whitman, *J. Vac. Sci. Technol. A*, **14**, 885 (1996).
16. B. Brar and D. Leonard, *Appl. Phys. Lett.* **66**, 463 (1995).

17. B. Brar, D. Leonard, and J.H. English, *Inst. Phys. Conf. Ser.* **141**, 335 (1995).
18. S. Subbanna *et al.*, *J. Vac. Sci. Technol. B*, **7**, 289 (1989).
19. J. Sudijono, M.D. Johnson, M.B. Elowitz, C.W. Snyder, and B.G. Orr, *Surf. Sci.* **280**, 247 (1993).
20. A.G. Milnes and A.Y. Polyakov, *Solid-State Electronics*, **36**, 803 (1993).
21. G.R. Johnson, B.C. Cavenett, T.M. Kerr, P.B. Kirby, and C.E.C. Wood, *Semicond. Sci. Technol.* **3**, 1157 (1988).
22. G.W. Turner, S.J. Eglash, and A.J. Strauss, *J. Vac. Sci. Technol. B*, **11**, 864 (1993).
23. P.S. Dutta, H.L. Bhat, and V. Kumar, *J. Appl. Phys.* **81**, 5821 (1997).
24. P.M. Thibado, B.R. Bennett, L.J. Whitman, B.V. Shanabrook, and R.J. Wagner (unpublished).
25. B.V. Shanabrook, D.S. Katzer, and R.J. Wagner, *Appl. Phys. Lett.* **59**, 1317 (1991).
26. J.J. Zinck and D.H. Chow, *Appl. Phys. Lett.* **66**, 3524 (1995).
27. J.J. Zinck, D.H. Chow, J.N. Schulman, and H.L. Dunlap *Appl. Phys. Lett.* **68**, 1406 (1996).
28. M. Weimer, B.V. Shanabrook, L.J. Whitman, and B.R. Bennett (unpublished).
29. E.A. Fitzgerald, Y. Ashizawa, L.F. Eastman, and D.G. Ast, *J. Appl. Phys.* **63**, 4925 (1988).
30. C.-A. Chang, H. Takoaka, L.L. Chang, and L. Esaki, *Appl. Phys. Lett.* **40**, 983 (1982).
31. R. Venkatasubramanian, D.L. Dorsey, and K. Mahalingam, *J. Cryst. Growth*, **175/176**, 224 (1997).
32. P.D. Brewer, D.H. Chow, and R.H. Miles, *J. Vac. Sci. Technol. B*, **14**, 2335 (1996).
33. Y. Rouillard, B. Lambert, Y. Toudic, M. Baudet, and M. Gauneau, *J. Cryst. Growth*, **156**, 30 (1995).
34. MBE source materials were Al: IHT Corporation, 7N; Sb: Dowa Mining Co., 7N+.
35. S. Ideshita, A. Furukawa, Y. Mochizuki, and M. Mizuta, *Appl. Phys. Lett.* **60**, 2549 (1992).
36. A. Furukawa and S. Ideshita, *J. Appl. Phys.* **75**, 5012 (1994).
37. C. Nguyen, B. Brar, H. Kroemer, and J. English, *J. Vac. Sci. Technol. B*, **10**, 898 (1992).
38. T.H. Chiu and W.T. Tsang, *J. Appl. Phys.* **57**, 4572 (1985).
39. J. Piao, R. Beresford, and W.I. Wang, *J. Vac. Sci. Technol. B*, **8**, 276 (1990).

40. G.E. Franklin *et al.*, *Phys. Rev. B*, **41**, 12619 (1990).
41. M. Yano, K. Yamamoto, T. Utatsu, and M. Inoue, *J. Vac. Sci. Technol. B*, **12**, 1133 (1994).
42. M.T. Sieger, T. Miller, and T.-C. Chiang, *Phys. Rev. B*, **52**, 8256 (1995).
43. P.M. Thibado, B.R. Bennett, B.V. Shanabrook, and L.J. Whitman, *J. Cryst. Growth*, **175/176**, 317 (1997).
44. L.J. Whitman, P.M. Thibado, S.C. Erwin, B.R. Bennett, B.V. Shanabrook, *Phys. Rev. Lett.* **79**, 693 (1997).
45. Earlier work suggested a narrow transition region with a (1×5) reconstruction.[41,43] Our recent STM studies indicate that the appearance of a (1×5) reconstruction in RHEED reflects a disordered (2×5) surface rather than a distinct phase.
46. B.R. Bennett, M.J. Yang, and B.V. Shanabrook (unpublished).
47. I.N. Stranski and L. Krastanov, *Sitzungsber. Akad. Wiss. Wien, Math.-Naturwiss. K1 IIb*, **146**, 797 (1938).
48. E. Bauer, *Z. Kristallogr.* **110**, 372 (1958).
49. R.W. Vook, *Opt. Eng.* **23**, 343 (1984).
50. R. Notzel, *Semicond. Sci. Technol.* **11**, 1365 (1996).
51. W. Seifert *et al.*, *Prog. Cryst. Growth and Charact.* **33**, 423 (1996).
52. B.A. Joyce and D.D. Vvedensky, This Volume, Ch. 8.
53. X. Zhang *et al.*, *J. Appl. Phys.* **67**, 800 (1990).
54. J. Drucker, *Phys. Rev. B*, **48**, 18203 (1993).
55. Y. Watanabe, T. Scimeca, F. Maeda, and M. Oshima, *Jpn. J. Appl. Phys.* **33**, 698 (1994).
56. F. Hatami *et al.*, *Appl. Phys. Lett.* **67**, 656 (1995).
57. B.R. Bennett, R. Magno, and B.V. Shanabrook, *Appl. Phys. Lett.* **68**, 505 (1996).
58. C.-K. Sun, G. Wang, J. E. Bowers, B. Brar, H.-R. Blank, H. Kroemer, and M. H. Pilkuhn *Appl. Phys. Lett.* **68**, 1543 (1996).
59. A.F. Tsatsul'nikov *et al.*, *Semiconductors*, **31**, 55 (1997).
60. N. Bertru, O. Brandt, M. Wassermeier, and K. Ploog, *Appl. Phys. Lett.* **68**, 31 (1996).
61. J.C. Ferrer *et al.*, *Appl. Phys. Lett.* **69**, 3887 (1996).
62. B.R. Bennett, P.M. Thibado, M.E. Twigg, E.R. Glaser, R. Magno, B.V. Shanabrook, and L.J. Whitman, *J. Vac. Sci. Technol. B*, **14**, 2195 (1996).
63. E.R. Glaser, B.R. Bennett, B.V. Shanabrook, and R. Magno, *Appl. Phys. Lett.* **68**, 3614 (1996).
64. Our PL measurements never show the wetting layer and QD bands in the same sample. This suggests that all the carriers are diffusing from the

wetting layer into the QDs before recombining. Perhaps for the Hatami *et al.* sample the diffusion lengths of electrons and holes are smaller than the typical distance between QDs. In the case of InAs/GaAs QDs, either one or two PL peaks can be observed depending on the growth conditions.
65. M.E. Rubin, H.R. Blank, M.A. Chin, H. Kroemer, and V. Narayanamurti, *Appl. Phys. Lett.* **70**, 1590 (1997).
66. B.R. Bennett, B.V. Shanabrook, and R. Magno, *Appl. Phys. Lett.* **68**, 958 (1996).
67. B.R. Bennett, B.V. Shanabrook, E.R. Glaser, R. Magno, and M.E. Twigg, *Superlatt. Microstr.* **21**, 267 (1997).
68. In bulk $Al_xGa_{1-x}Sb$ at 300 K, the energy of the AlSb-like mode increases from 319 cm^{-1} (x=0) to 334 cm^{-1} (x=1), while the energy of the GaSb-like mode decreases from 235 cm^{-1} (x=0) to 212 cm^{-1} (x=1); see D.H. Jaw, D.S. Cao, and G.B. Stringfellow, *J. Appl. Phys.* **69**, 2552 (1991).
69. G. Armelles *et al.*, *J. Appl. Phys.* **81**, 6339 (1997).
70. C. Priester and M. Lannoo, *Phys. Rev. Lett.* **75**, 93 (1995).
71. C. Ratsch, P. Smilauer, D.D. Vvedensky, and A. Zangwill, *J. Phys. I France* **6**, 575 (1996).
72. B.R. Bennett, B.V. Shanabrook, P.M. Thibado, L.J. Whitman, and R. Magno, *J. Cryst. Growth*, **175/176**, 888 (1997).
73. J.W. Matthews and A.E. Blakeslee, *J. Cryst. Growth*, **27**, 118 (1974).
74. H.-J. Gossmann *et al.*, *J. Appl. Phys.* **66**, 1687 (1989).
75. J.L. Lazzari, C. Fouillant, P. Grunberg, J.L. Leclercq, A. Joullie, and C. Schiller, *J. Cryst. Growth*, **130**, 96 (1993).
76. B.R. Bennett, submitted to *Appl. Phys. Lett.*
77. Although the value of $\Delta\theta$ for the 2000 Å layer (1580 arc-sec) is very close to the theoretical value for a coherent layer, the values for 500 and 1000 Å layers, 1450 and 1480 arc-sec, respectively, are somewhat smaller. This discrepancy is beyond the experimental uncertainty and was reproduced with single-crystal x-ray measurements. Several possibilities have been considered, including the Fewster-Curling effect, slightly off-orientation substrates, errors in Poisson's ratio, and Ga contamination in the InAs, but none appear to be large enough to account for the discrepancy.
78. I.J. Fritz, *Appl. Phys. Lett.* **51**, 1080 (1987).
79. C.R. Wie, *J. Appl. Phys.* **65**, 2267 (1989).
80. B.R. Bennett and J.A. del Alamo, *J. Appl. Phys.* **73**, 3195 (1993).
81. J.F. Klem, W.S. Fu, P.L. Gourley, E.D. Jones, T.M. Brennan, and J.A. Lott, *Appl. Phys. Lett.* **56**, 1350 (1990).
82. M. Meshkinpour, M.S. Goorsky, B. Jenichen, D.C. Streit, and T.R.

Block, *J. Appl. Phys.* **81**, 3124 (1997).
83. B.V. Shanabrook, J.R. Waterman, J.L. Davis, and R.J. Wagner, *Appl. Phys. Lett.* **61**, 2338 (1992).
84. B.V. Shanabrook, J.R. Waterman, J.L. Davis, R.J. Wagner, and D.S. Katzer, *J. Vac. Sci. Technol. B*, **11**, 994 (1993).
85. M. Yano, H. Yokose, Y. Iwai, and M. Inoue, *J. Cryst. Growth*, **111**, 609 (1991).
86. C.E.C. Wood in *InGaAsP Alloy Semiconductors*, p. 91, ed. T.P. Pearsall (Wiley, New York, 1982).
87. B.R. Bennett, B.V. Shanabrook, and M.E. Twigg, submitted to *J. Cryst. Growth.*
88. M.W. Wang, D.A. Collins, T.C. McGill, and R.W. Grant, *J. Vac. Sci. Technol. B*, **11**, 1418 (1993).
89. D.A. Collins, M.W. Wang, R.W. Grant, and T.C. McGill, *J. Vac. Sci. Technol. B*, **12**, 1125 (1994).
90. B.V. Shanabrook and B.R. Bennett, *Phys. Rev. B*, **50**, 1695 (1994).
91. B.V. Shanabrook and B.R. Bennett, *Proc. 22nd Intl. Conf. Phys. Semicond.* p. 955, (World Scientific Publishing, Singapore, 1995).
92. R. Perez-Alvarez and C. Trallero-Giner, *Physica Scripta*, **56**, 407 (1997).
93. B.V. Shanabrook, B.R. Bennett, and R.J. Wagner, *Phys. Rev. B*, **48**, 17172 (1993).
94. A. Fasolino, E. Molinari, and J.C. Maan, *Phys. Rev. B*, **33**, 8889 (1986) and **39**, 3923 (1989).
95. D.H. Chow, Y.H. Zhang, R.H. Miles, and H.L. Dunlap, *J. Cryst. Growth*, **150**, 879 (1995).
96. C.R. Bolognesi, J.E. Bryce, and D.H. Chow, *Appl. Phys. Lett.* **69**, 3531 (1996).
97. B.R. Bennett, B.V. Shanabrook, E.R. Glaser, and R.J. Wagner, *Mater. Res. Soc. Proc.* **340**, 253 (1994).
98. B.R. Bennett, B.V. Shanabrook, and E.R. Glaser, *Appl. Phys. Lett.* **65**, 598 (1994).
99. Z. Dobrovolskis, K. Grigoras, and A. Krotkus, *Appl. Phys. A*, **48**, 245 (1989).
100. S.V. Ivanov and P.S. Kop'ev, in *Antimonide Related Strained-Layer Heterostructures*, pp. 95–170, ed. M. O. Manasreh (Gordon and Breach, Amsterdam, 1997).
101. A.G. Milnes and A.Y. Polyakov, *Mater. Sci. Eng. B*, **18**, 237 (1993).
102. G. Tuttle, H. Kroemer, and J.H. English, *J. Appl. Phys.* **65**, 5239 (1989).
103. G. Tuttle, H. Kroemer, and J.H. English, *J. Appl. Phys.* **67**, 3032

(1990).
104. C.R. Bolognesi, H. Kroemer, and J.H. English, *J. Vac. Sci. Technol. B*, **10**, 877 (1992).
105. C.R. Bolognesi, H. Kroemer, and J.H. English, *Appl. Phys. Lett.* **61**, 213 (1992).
106. C. Nguyen, B. Brar, C.R. Bolognesi, J.J. Pekarik, H. Kroemer, and J.H. English, *J. Electr. Mater.* **22**, 255 (1993).
107. H.-R. Blank, M. Thomas, K.C. Wong, and H. Kroemer, *Appl. Phys. Lett.* **69**, 2080 (1996).
108. J.B. Boos, W. Kruppa, D. Park, B. Molnar, and B.R. Bennett, *Electr. Lett.* **32**, 688 (1996).
109. J.D. Werking, C.R. Bolognesi, L.-D. Chang, C. Nguyen, E.L. Hu, and H. Kroemer, *IEEE Electr. Dev. Lett.* **13**, 164 (1992).
110. T.A. Malik, S.J. Chung, R.A. Stradling, W.T. Yuen, J.J. Harris, and A.G. Norman, *Inst. Phys. Conf. Ser.* **144**, 229 (1995).
111. B.R. Bennett, M.J. Yang, and B.V. Shanabrook, J.B. Boos, and D. Park, *Appl. Phys. Lett.* **72**, 1193 (1998).
112. S. Sasa, Y. Yamamoto, S. Izumiya, M. Yano, Y. Iwai, and M. Inoue, *Jpn. J. Appl. Phys.* **36**, 1869 (1997).
113. X. Li, K.F. Longenbach, Y. Wang, W.I. Wang, *IEEE Electr. Dev. Lett.* **13**, 192 (1992).
114. C.R. Bolognesi, E.J. Caine, and H. Kroemer, *IEEE Electr. Dev. Lett.* **15**, 16 (1994).
115. K. Yoh, T. Moriuchi, and M. Inoue, *Jpn. J. Appl. Phys.* **29**, L2445 (1990).
116. J.B. Boos, W. Kruppa, D. Park, B.V. Shanabrook, and B.R. Bennett, *Electr. Lett.* **30**, 1983 (1994).
117. W. Kruppa, J.B. Boos, D. Park, B.R. Bennett, and R. Bass, *Electr. Lett.* **33**, 1092 (1997).
118. J.B. Boos, W. Kruppa, B.R. Bennett, D. Park, S. Kirchoefer, R. Bass, and H.B. Dietrich, submitted to *IEEE Trans. Electr. Dev.*
119. L.L. Chang, N.J. Kawai, G.A. Sai-Halasz, R. Ludeke, and L. Esaki, *Appl. Phys. Lett.* **35**, 939 (1979).
120. Y. Guldner, J.P. Vieren, P. Voisin, M. Voos, L.L. Chang, and L. Esaki, *Phys. Rev. Lett.* **45**, 1719 (1980).
121. L.M. Claessen, J.C. Maan, M. Altarellli, P. Wyder, L.L. Chang, and L. Esaki, *Phys. Rev. Lett.* **57**, 2556 (1986).
122. M.S. Daly, D.M. Symons, M. Lakrimi, R.J. Nicholas, N.J. Mason, and P.J. Walker, *Semicond. Sci. Technol.* **11**, 823 (1996).
123. J.R. Waterman, B.V. Shanabrook, R.J. Wagner, M.J. Yang, J.L. Davis,

and J.P. Omaggio, *Semicond. Sci. Technol.* **8**, S106 (1993).
124. L.A. Hemstreet, C.Y. Fong, and J.S. Nelson, *J. Vac. Sci. Technol. B*, **11**, 1693 (1993).
125. R.J. Wagner, B.V. Shanabrook, M.J. Yang, and J.R. Waterman, *Superlatt. Microstr.* **21**, 95 (1997).
126. J.R. Meyer, C.A. Hoffman, B.V. Shanabrook, B.R. Bennett, R.J. Wagner, J.R. Waterman, and E.R. Youngdale, *Proc. 22nd Intl. Conf. Phys. Semic.* p. 793, (World Scientific Publishing, Singapore, 1995).
127. M.W. Wang, D.A. Collins, T.C. McGill, R.W. Grant, and R.M. Feenstra, *Appl. Phys. Lett.* **66**, 2981 (1995).
128. B. Montanari, M. Peressi, S. Baroni, and E. Molinari, *Appl. Phys. Lett.* 69, 3218 (1996).
129. M. Altarelli, *Phys. Rev. B*, **28**, 842 (1983).
130. A. Fasolino and M. Altarelli, *Surf. Sci.* **142**, 322 (1984).
131. M. Altarelli, J.C. Maan, L.L. Chang, and L. Esaki, *Phys. Rev. B*, **35**, 9867 (1987).
132. M.S. Daly *et al.*, *Phys. Rev. B*, **53**, R10524 (1996).
133. J. Kono, B.D. McCombe, J.-P. Cheng, I. Lo, W.C. Mitchel, and C.E. Stutz, *Phys. Rev. B*, **55**, 1617 (1997).
134. R.J. Wagner and B.V. Shanabrook (unpublished).
135. J.-C. Chiang, S.-F. Tsay, Z.M. Chau, and I. Lo, *Phys. Rev. Lett.* **77**, 2053 (1996).
136. M.J. Yang, C.H. Yang, B.R. Bennett, and B.V. Shanabrook, *Phys. Rev. Lett.* **78**, 4613 (1997).
137. M. Lakrimi *et al.*, *Phys. Rev. Lett.* **79**, 3034 (1997).
138. D.L. Smith and C. Mailhiot, *J. Appl. Phys.* **62**, 2545 (1987).
139. HgCdTe Ref.
140. B.R. Bennett, B.V. Shanabrook, R.J. Wagner, J.L. Davis, and J.R. Waterman, *Appl. Phys. Lett.* **63**, 949 (1993).
141. J.L. Davis, R.J. Wagner, J.R. Waterman, B.V. Shanabrook, and J.P. Omaggio, *J. Vac. Sci. Technol. B*, **11**, 861 (1993).
142. D.H. Chow, R.H. Miles, J.R. Soderstrom and T.C. McGill, *Appl. Phys. Lett.* **56**, 1418 (1990).
143. C. Lopez, R.J. Springett, R.J. Nicholas, P.J. Walker, N.J. Mason, and W. Hayes, *Surf. Sci.* **267**, 176 (1992).
144. I. Sela, L.A. Samoska, C.R. Bolognesi, A.C. Gossard, and H. Kroemer, *Phys. Rev. B*, **46**, 7200 (1992).
145. M.E. Twigg, B.R. Bennett, P.M. Thibado, B.V. Shanabrook, and L.J. Whitman, in *Antimonide Related Strained-Layer Heterostructures*, pp. 55–93, ed. M. O. Manasreh (Gordon and Breach, Amsterdam, 1997).

146. S.G. Lyapin. P.C. Klipstein, N.J. Mason, and P.J. Walker, *Phys. Rev. Lett.* **74**, 3285 (1995).
147. B.C. De Cooman C.B. Carter, G.W. Wicks, T. Tanoue, and L.F. Eastman, *Thin Solid Films*, **170**, 49 (1989).
148. M.E. Twigg, B.R. Bennett, B.V. Shanabrook, J.R. Waterman, J.L. Davis, and R.J. Wagner, *Appl. Phys. Lett.* **64**, 3476 (1994).
149. M.E. Twigg, B.R. Bennett, and B.V. Shanabrook, *Appl. Phys. Lett.* **67**, 1609 (1995).
150. M.E. Twigg, B.R. Bennett, P.M. Thibado, B.V. Shanabrook, and L.J. Whitman, *Phil. Mag. A* **76**, 7 (1998).
151. R.M. Feenstra, D.A. Collins, D.Z.-Y. Ting, M.W. Wang, and T.C. McGill, *Phys. Rev. Lett.* **72**, 2749 (1994); *J. Vac. Sci. Technol. B*, **12**, 2592 (1994).
152. A.Y. Lew, E.T. Yu, D.H. Chow, and R.H. Miles, *Appl. Phys. Lett.* **65**, 201 (1994).
153. A.Y. Lew, S.L. Zuo, E.T. Yu, and R.H. Miles, *Appl. Phys. Lett.* **70**, 75 (1997).
154. P.M. Thibado, B.R. Bennett, M.E. Twigg, B.V. Shanabrook, and L.J. Whitman, *Appl. Phys. Lett.* **67**, 3578 (1995).
155. N. Herres *et al.*, *Phys. Rev. B*, **53**, 15688 (1996).
156. F. Fuchs, J. Wagner, J. Schmitz, N. Herres, and P. Koidl in *Antimonide Related Strained-Layer Heterostructures*, pp.171–234, ed. M. O. Manasreh (Gordon and Breach, Amsterdam, 1997).
157. B.R. Bennett, B.V. Shanabrook, R.J. Wagner, J.L. Davis, J.R. Waterman, and M.E. Twigg, *Solid-State Electr.* **37**, 733 (1994).
158. D.H. Chow, R.H. Miles, and A.T. Hunter, *J. Vac. Sci. Technol. B*, **10**, 888 (1992).
159. C. Gadaleta, G. Scamarcio, F. Fuchs, and J. Schmitz, *J. Appl. Phys.* **78**, 5642 (1995).
160. M.J. Yang and B.R. Bennett, *Electr. Lett.* **30**, 1710 (1994).
161. H. Mohseni, E. Michel, J. Sandoen, M. Razeghi, W. Mitchel, and G. Brown, *Appl. Phys. Lett.* **71**, 1403 (1997).
162. M.D. Jack *et al.*, *Proc. IRIS Detector Workshop*, 205 (1993).
163. J.L. Johnson, L. A. Samoska, A. C. Gossard, J. L. Merz, M. D. Jack, G. R. Chapman, B. A. Baumgratz, K. Kosai, and S. M. Johnson, *J. Appl. Phys.* **80**, 1116 (1996).
164. F. Fuchs *et al.*, *Proc. 8th Intl. Conf. Narrow Gap Semiconductors*, (World Scientific Publishing, Singapore, 1997).
165. F. Fuchs, U. Weimer, W. Pletschen, J. Schmitz, E. Ahlswede, M. Walther, J. Wagner, and P. Koidl, *Appl. Phys. Lett.* **71**, 3251 (1997).